Structural evolution in A ≈100 nuclei within the mapped interacting boson model based on the Gogny energy density functional

Nomura, Kosuke; Rodriguez-Guzmán, R.; Robledo, L. M.

Download date / Datum preuzimanja: **2025-01-26**

Repository / Repozitorij:

Repository of the Faculty of Science - University of Zagreb

Structural evolution in $A \approx 100$ nuclei within the mapped interacting boson model based on the Gogny energy density functional

K. Nomura,[1,2] R. Rodríguez-Guzmán,[3] and L. M. Robledo[4]

[1]*Physics Department, Faculty of Science, University of Zagreb, HR-10000 Zagreb, Croatia*
[2]*Center for Computational Sciences, University of Tsukuba, Tsukuba 305-8577, Japan*
[3]*Physics Department, Kuwait University, 13060 Kuwait, Kuwait*
[4]*Departamento de Física Teórica, Universidad Autónoma de Madrid, E-28049 Madrid, Spain*

The structure of even-even neutron-rich Ru, Mo, Zr, and Sr nuclei in the $A \approx 100$ mass region is studied within the interacting boson model (IBM) with microscopic input from the self-consistent mean-field approximation based on the Gogny-D1M energy density functional. The deformation-energy surface in the quadrupole deformation space (β, γ), computed within the constrained Hartree–Fock–Bogoliubov framework, is mapped onto the expectation value of the appropriately chosen IBM Hamiltonian with configuration mixing in the boson condensate state. The mapped IBM Hamiltonian is used to study the spectroscopic properties of $^{98-114}$Ru, $^{96-112}$Mo, $^{94-110}$Zr, and $^{92-108}$Sr. Several cases of γ-soft behavior are predicted in Ru and Mo nuclei while a pronounced coexistence between strongly prolate and weakly oblate deformed shapes is found for Zr and Sr nuclei. The method describes well the evolution of experimental yrast and nonyrast states as well as selected $B(E2)$ transition probabilities.

I. INTRODUCTION

The study of collective excitations and the associated shapes in nuclei with mass number $A \approx 100$ has received lately considerable attention in nuclear structure physics [1]. As a consequence of the subtle interplay between single-particle and collective degrees of freedom, nuclei in this region of the nuclear chart display a large variety of intriguing phenomena. Several experimental [2–8] and theoretical [9–17] studies have already been reported on the structure of these nuclei. In particular, the rapid structural change around the neutron number $N = 60$ has been carefully studied in Zr and Sr isotopes [2,7,12,14,15,18–20]. This mass region is also characterized by the competition between different low-lying configurations based on different intrinsic deformations, i.e., shape coexistence [1,7,8,12,14,20].

Both the nuclear shell-model (SM) [21] and the energy density functional (EDF) [22] frameworks are among the most popular theoretical tools used to describe the structure of medium-mass and heavy nuclei. On the one hand, the SM calculations encode the most important correlations for the considered nuclei and provide access to their spectroscopic properties. However, for open-shell systems, the dimension of the SM Hamiltonian matrix becomes exceedingly large making its diagonalization prohibitively expensive. On the other hand, the EDF scheme [22–24] yields a global description of nuclear matter and bulk nuclear properties. Within this context, the evolution of the nuclear shapes around $A = 100$ has been studied by using self-consistent mean-field (SCMF) approximations based on different parametrizations of the Skyrme [25] and Gogny [7,12] as well as relativistic [14,15,26] EDFs. However, in order to access the excitation spectra and transition rates within the EDF scheme, one needs to go beyond the mean-field level to include dynamical correlations associated with the restoration of the broken symmetries and/or the fluctuations in the collective coordinates. Such a task is usually accounted for via symmetry-projected configuration-mixing calculations within the generator coordinate method (GCM) framework [22,24,27,28]. However, symmetry-projected GCM calculations are also computationally demanding in the case of heavy nuclear systems, especially when several collective coordinates (quadrupole, octupole, pairing, etc.) have to be taken into account as generating coordinates.

In this work, we resort to an alternative approach, which is based on mapping the considered EDF into an algebraic model of interacting bosons [29]. Our starting point is the (constrained) SCMF approximation that provides the corresponding microscopic energy surface as a function of the relevant deformation parameters. Such a surface is subsequently mapped onto the expectation value of the interacting boson model (IBM) [30] Hamiltonian computed with the boson condensate state. The parameters of the IBM Hamiltonian are determined from such a mapping procedure. The resulting IBM Hamiltonian is then used to obtain the excitation spectra and electromagnetic transition rates. The method allows a computationally feasible as well as quantitative description of the low-energy collective excitations. It has already been applied to study the quadrupole [29,31–33] and octupole [34] modes in atomic nuclei as well as to describe shape-coexistence phenomena [35–37]. In the present study we extend the method of Ref. [29] to study the challenging structural evolution and shape coexistence in neutron-rich nuclei with $A \approx 100$. The nuclei $^{92-108}$Sr, $^{94-110}$Zr, $^{96-112}$Mo, and $^{98-114}$Ru have been taken as a representative sample. The phenomenological IBM framework has been applied to describe some of those nuclei in the past [10,11,38–41]. However, even when several attempts have been made [4,10,11] to extrapolate the IBM scheme to unknown regions of the periodic table, in most of the cases the model has not been extensively used to predict the

properties of exotic nuclei. Within this context, one of the main advantages of our method over the conventional phenomenological IBM approaches is that it predicts the properties of unexplored nuclei based only on the underlying microscopic EDF framework. Our SCMF calculations are based on the Gogny-D1M [42,43] EDF. Previous studies [44–48] have shown that the parameter set D1M essentially keeps the same predictive power of the more traditional Gogny-D1S [49] EDF regarding a wealth of low-energy nuclear structure properties while improving the description of the nuclear masses [43]. The Gogny-D1M EDF has also been applied to the study of nuclei, including the odd-mass ones, in the $A \approx 100$ mass region [3,4,12,13].

The paper is organized as follows: In Sec. II we briefly outline the theoretical framework used in this work. The results of our calculations are presented in Sec. III, where we discuss the deformation-energy surfaces and the IBM parameters derived from our mapping procedure. In the same section we consider the evolution of the low-lying levels in the studied nuclei as well as the systematics of the $B(E2)$ transition rates. We also discuss the individual level schemes for $N = 60$ isotones. The robustness of our method is addressed by studying specifically the sensitivity of the results to variations on key parameters. Finally, Sec. IV is devoted to the concluding remarks.

II. THEORETICAL FRAMEWORK

A. Constrained self-consistent mean-field calculations

As already mentioned above, the first step in our calculations is to obtain the deformation-energy surfaces for the considered nuclei. To this end, we have performed constrained Hartree–Fock–Bogoliubov (HFB) calculations based on the Gogny-D1M EDF. We have resorted to constraints on the $\hat{Q}_{20}$ and $\hat{Q}_{22}$ operators [44,50]. The quadrupole moment is then defined as $Q = \sqrt{Q_{20} + Q_{22}}$. We then consider the deformation parameters $\beta = \sqrt{4\pi/5} Q / \langle r^2 \rangle$ and $\gamma = \tan^{-1} Q_{22}/Q_{20}$. In the definition of β the mean-square radius $\langle r^2 \rangle$ is evaluated with the corresponding HFB state. For more details on the constrained Gogny-HFB framework the reader is referred, for example, to Ref. [44]. In what follows, we refer to the total mean-field energy as a function of the (β, γ) parameters as the deformation-energy surface.

B. Interacting boson model with configuration mixing

To compute the excitation spectra and transition rates, we use the method of Ref. [29] in which the parameters of the IBM Hamiltonian are determined by mapping the deformation-energy surface provided by the constrained Gogny-D1M SCMF calculations onto the expectation value of the IBM Hamiltonian computed the boson condensate (intrinsic) wave function [51]. The resulting IBM Hamiltonian is then used to calculate spectroscopic properties for the studied nuclei. We consider the proton-neutron IBM (denoted IBM-2) [52,53] because it represents a more realistic approach that is able to treat both the proton and neutron degrees of freedom. The building blocks of the IBM-2 model are the correlated monopole 0^+ (S_π and S_ν) and quadrupole 2^+ (D_π and D_ν)

pairs of valence protons (π) and neutrons (ν). The S_π (S_ν) and D_π (D_ν) pairs are associated with the proton (neutron) s_π (s_ν) and d_π (d_ν) bosons, which have spin and parity $J^\pi = 0^+$ and 2^+, respectively [53]. The number of proton (N_π) and neutron (N_ν) bosons is equal to half the number of valence protons and neutrons [52,53]. The bosonic model space comprises the neutron major shell $N = 50$–82 and the proton $Z = 40$–50 shell for Ru, Mo, and Zr isotopes and $Z = 28$–40 in the case of Sr isotopes. Therefore, $2 \leqslant N_\nu \leqslant 8$ for the nuclei studied while $N_\pi = 0$ (Zr), 1 (Sr and Mo), and 2 (Ru).

As will be shown, for many of the nuclei in the selected sample, the Gogny-D1M energy surface exhibits up to three mean-field minima close in energy to each other. Accordingly, the bosonic model space should be extended so as to take into account those configurations. In a mean-field picture, the different mean-field minima are associated with $2n$-particle-$2n$-hole ($n = 0, 1, 2$) intruder excitations across the closed shell. To incorporate the intruder configurations, we follow the method of Duval and Barrett [54], which associates the different SM-like spaces of $0p$-$0h$, $2p$-$2h$, $4p$-$4h$, ... excitations with the corresponding boson spaces comprising N_B, $N_B + 2$, $N_B + 4$, ... bosons, where $N_B (= N_\nu + N_\pi)$ denotes the total number of bosons. The different boson subspaces are allowed to mix by introducing an additional interaction. Under the assumption of Duval and Barrett, particles and holes are not distinguished. Then, as the excitation of one pair (boson) increases the boson number by two, the configurations for the $2np$-$2nh$ excitations differ from each other in boson number by two. In the following, we assume only the proton ph excitations across the subshell closure $Z = 40$, which is equivalent to the excitation from the proton pf shell to the $1g_{9/2}$ orbital. The Hilbert space for the configuration-mixing IBM-2 model is then defined as the direct sum of each "unperturbed" configuration space, i.e.,

$$[N_\nu \otimes N_\pi] \oplus [N_\nu \otimes (N_\pi + 2)] \oplus [N_\nu \otimes (N_\pi + 4)], \quad (1)$$

where $[N_\nu \otimes (N_\pi + 2n)]$ ($n = 0, 1,$ and 2) denotes the configuration space for the unperturbed IBM-2 Hamiltonian for the $2np$–$2nh$ proton excitations, comprising N_ν neutron and $N_\pi + 2n$ proton bosons. In the following, the unperturbed space $[N_\nu \otimes (N_\pi + 2n)]$ is simply denoted as $[n]$ ($n = 0, 1,$ and 2), and we refer to the IBM-2 simply as IBM, unless otherwise specified.

The Hamiltonian $\hat{H}_B$ for the system is then expressed in terms of up to three unperturbed IBM Hamiltonians $\hat{H}_n$ ($n = 0$, 1, and 2) differing in boson number by two and in terms of $\hat{H}_{n,n+1}^{\text{mix}}$ that mix different boson subspaces:

$$\hat{H}_B = \hat{H}_0 + (\hat{H}_1 + \Delta_1) + (\hat{H}_2 + \Delta_2) + \hat{H}_{0,1}^{\text{mix}} + \hat{H}_{1,2}^{\text{mix}}, \quad (2)$$

where Δ_1 and Δ_2 represent the energies required to excite one and two bosons across the inert core.

For the unperturbed Hamiltonian $\hat{H}_n$ ($n = 0, 1,$ and 2) we have taken the form

$$\hat{H}_n = \epsilon_n \hat{n}_d + \kappa_n \hat{Q} \cdot \hat{Q} + \kappa_n' \sum_{\rho' \neq \rho} \hat{T}_{\rho\rho'}, \quad (3)$$

where the first term $\hat{n}_d = \hat{n}_{d\nu} + \hat{n}_{d\pi}$, where $\hat{n}_{d\rho} = d_\rho^\dagger \cdot \tilde{d}_\rho$ ($\rho = \nu, \pi$) represents the d-boson number operator. On the

other hand, $\hat{Q} = \hat{Q}_\nu + \hat{Q}_\pi$ is the quadrupole operator and $\hat{Q}_\rho = s_\rho^\dagger \tilde{d}_\rho + d_\rho^\dagger \tilde{s}_\rho + \chi_{\rho,n}[d_\rho^\dagger \times \tilde{d}_\rho]^{(2)}$. The third term is a specific three-boson interaction with $\hat{T}_{\rho\rho'} = \sum_L [d_\rho^\dagger \times d_\rho^\dagger \times d_{\rho'}^\dagger]^{(L)} \cdot [\tilde{d}_{\rho'} \times \tilde{d}_\rho \times \tilde{d}_\rho]^{(L)}$, where L denotes the total angular momentum in the boson system.

The mixing interaction reads

$$\hat{H}_{n,n+1}^{\mathrm{mix}} = \omega_{s,n} s_\pi^\dagger \cdot s_\pi^\dagger + \omega_{d,n} d_\pi^\dagger \cdot d_\pi^\dagger + \mathrm{H.c.}, \qquad (4)$$

where $\omega_{s,n}$ and $\omega_{d,n}$ are strength parameters and are assumed to be equal ($\omega_{s,n} = \omega_{d,n} = \omega_n$) for simplicity. Note that there is no direct coupling between the $[n=0]$ and $[n=2]$ spaces with the two-body nuclear interactions.

The unperturbed Hamiltonian $\hat{H}_n$ in Eq. (3) takes the simplest form of the sd-IBM-2 Hamiltonian used for describing low-energy quadrupole collective states. It is only composed of $\hat{n}_d$ and $\hat{Q}_\nu \cdot \hat{Q}_\pi$ terms [29,53,55]. The addition of the like neutron boson term $\hat{Q}_\nu \cdot \hat{Q}_\nu$ in Eq. (3) is due to the fact that, in the present study, $N_\pi = 0$ for the normal (or $0p$–$0h$) configuration of the Zr isotopes and, without this term, the SCMF minimum could not be reproduced. We also include the interaction term between like proton bosons $\hat{Q}_\pi \cdot \hat{Q}_\pi$ and, to reduce the number of parameters, assume the F-spin [52,56] invariant form for the quadrupole operator $\hat{Q} = \hat{Q}_\nu + \hat{Q}_\pi$. On the other hand, the three-boson term is required to describe a triaxial minimum. We only consider the interaction between proton and neutron bosons with $L = 3$. The specific choice of the three-boson term is due to the relevance of the proton-neutron interactions in medium-mass and heavy nuclei, and that only the $L = 3$ term gives rise to a stable triaxial minimum at $\gamma \approx 30°$ [33]. For those nuclei where the configuration mixing is taken into account, the strength parameter κ' is taken to be equal to that of the quadrupole-quadrupole term, i.e., $\kappa' = \kappa$. For the nuclei where the configuration mixing is not considered, κ' is taken as an independent parameter.

To look at the geometrical feature of the configuration-mixing IBM Hamiltonian $\hat{H}_B$, we introduce the following boson intrinsic state $|\Phi_B(\beta,\gamma)\rangle$, extended to the space $[n = 0] \oplus [n = 1] \oplus [n = 2]$:

$$|\Phi_B(\beta,\gamma)\rangle = |\Phi_B(0,\beta,\gamma)\rangle \oplus |\Phi_B(1,\beta,\gamma)\rangle \oplus |\Phi_B(2,\beta,\gamma)\rangle. \qquad (5)$$

The coherent state for each unperturbed space $|\Phi_B(n,\beta,\gamma)\rangle$ ($n = 0$, 1, and 2) reads

$$|\Phi(n,\beta,\gamma)\rangle = \frac{1}{\sqrt{N_\nu! N_{\pi,n}!}}(\lambda_\nu^\dagger)^{N_\nu}(\lambda_\pi^\dagger)^{N_{\pi,n}}|0\rangle, \qquad (6)$$

with $N_{\pi,n} \equiv N_\pi + 2n$ and

$$\lambda_\rho = s_\rho^\dagger + \beta_\rho \cos\gamma_\rho d_0^\dagger + \tfrac{1}{2}\beta_\rho \sin\gamma_\rho(d_{+2}^\dagger + d_{-2}^\dagger). \qquad (7)$$

β_ρ and γ_ρ are the quadrupole deformation parameters analogous to those in the collective model [57]. They are assumed to be the same between protons and neutrons, i.e., $\beta_\nu = \beta_\pi \equiv \beta_B$ and $\gamma_\nu = \gamma_\pi \equiv \gamma_B$. The bosonic deformation parameters β_B and γ_B could be related to those in the collective model in such a way that $\beta_B \propto \beta$ and $\gamma_B = \gamma$ [51].

The expectation value of the total Hamiltonian $\hat{H}_B$ in the coherent state $|\Phi_B(\beta,\gamma)\rangle$ leads us to consider the 3×3 matrix [58]:

$$\mathcal{E} = \begin{pmatrix} E_0(\beta,\gamma) & \Omega_{0,1}(\beta) & 0 \\ \Omega_{1,0}(\beta) & E_1(\beta,\gamma) + \Delta_1 & \Omega_{1,2}(\beta) \\ 0 & \Omega_{2,1}(\beta) & E_2(\beta,\gamma) + \Delta_2 \end{pmatrix}, \qquad (8)$$

where the diagonal and off-diagonal elements represent the expectation values of the unperturbed Hamiltonians and the mixing interactions, respectively. The three eigenvalues of $\mathcal{E}$ correspond to specific energy surfaces depending on the values of the parameters, and it is customary to take the lowest-energy one [58] as the IBM deformation energy at each deformation (β,γ).

The analytical expression of the diagonal matrix element $E_n(\beta,\gamma)$ ($n = 0$, 1, and 2) is given as

$$E_n(\beta,\gamma) = \frac{k_1 + k_2\beta_{B,n}^2}{1 + \beta_{B,n}^2} + \frac{k_3\beta_{B,n}^2 + k_4\beta_{B,n}^3\cos 3\gamma + k_5\beta_{B,n}^4}{(1 + \beta_{B,n}^2)^2} + \frac{k_6\beta_{B,n}^3\sin^2 3\gamma}{(1 + \beta_{B,n}^2)^3}, \qquad (9)$$

where

$$k_1 = 5\kappa_n(N_\nu + N_{\pi,n}),$$
$$k_2 = \left[\epsilon_n + \kappa_n(1 + \chi_{\nu,n}^2)\right]N_\nu + \left[\epsilon_n + \kappa_n(1 + \chi_{\pi,n}^2)\right]N_{\pi,n},$$
$$k_3 = 4\kappa_n(N_\nu + N_{\pi,n})(N_\nu + N_{\pi,n} - 1),$$
$$k_4 = -4\kappa_n\sqrt{\frac{2}{7}}(\chi_{\nu,n}N_\nu + \chi_{\pi,n}N_{\pi,n})(N_\nu + N_{\pi,n} - 1),$$
$$k_5 = \frac{2}{7}\kappa_n\left[(\chi_{\nu,n}N_\nu + \chi_{\pi,n}N_{\pi,n})^2 - (\chi_{\nu,n}^2N_\nu + \chi_{\pi,n}^2N_{\pi,n})\right],$$
$$k_6 = -\frac{1}{7}\kappa_n' N_\nu N_{\pi,n}(N_\nu + N_{\pi,n} - 2), \qquad (10)$$

and that of the nondiagonal matrix element $\Omega_{n,n+1}(\beta)$ ($n = 0$ and 1) as

$$\Omega_{n,n+1}(\beta) = \Omega_{n+1,n}(\beta)$$
$$= \omega_n\sqrt{(N_{\pi,n} + 1)N_{\pi,n+1}}$$
$$\times \left[\frac{1 + \beta_{B,n}\beta_{B,n+1}}{\sqrt{(1 + \beta_{B,n}^2)(1 + \beta_{B,n+1}^2)}}\right]^{N_\nu + N_{\pi,n}}. \qquad (11)$$

In both Eqs. (9) and (11), $\beta_{B,n}$ denotes the bosonic deformation parameter in each unperturbed space $[n]$ and is connected to the β deformation parameter of the SCMF model through the relation $\beta_{B,n} = C_n\beta$. The constant C_n is also determined from the energy-surface fitting procedure by requiring that the position of the minimum for each unperturbed configuration is reproduced. The formulas in Eqs. (9) and (11) are the same as those found in Ref. [36] except for the fact that, in the present study, the expectation value of the like-particle $\hat{Q}_\rho \cdot \hat{Q}_\rho$ term is also included whereas that of the rotational $\hat{L} \cdot \hat{L}$ term is not included.

C. The mapping procedure

All together the model has 22 parameters that have to be fixed. This represents too much freedom and therefore some of the parameters have been kept fixed to simplify the calculation. The fitting protocol used is the following:

(i) Each unperturbed Hamiltonian is determined by using the procedure of Refs. [29,31]: Each diagonal matrix element E_n in Eq. (8) is fit to the corresponding mean-field minimum. The normal [$n = 0$] configuration is assigned to the mean-field minimum with the smallest deformation [59]. On the other hand the [$n = 1$] ([$n = 2$]) configuration corresponds to the minimum with the second (third) smallest deformation. In this way, each unperturbed Hamiltonian is determined independently.

(ii) We then extract the energy offsets Δ_1 and Δ_2 so that the energy difference between the two neighboring minima on the Gogny-D1M energy surface is reproduced.

(iii) Finally, what is left is to introduce the mixing interactions $\hat{H}_{n,n+1}^{\mathrm{mix}}$ and determine the ω strengths. They could be determined so as to reproduce the topology of the barriers between the minima Refs. [35,36]. However, in this work we have assumed, for the sake of simplicity, a constant strength $\omega = 0.1$ MeV for both $\hat{H}_{0,1}^{\mathrm{mix}}$ and $\hat{H}_{1,2}^{\mathrm{mix}}$ terms, in order to keep the mixing interactions perturbative.

Once its parameters are determined, the Hamiltonian $\hat{H}_B$ is diagonalized in the [$n = 0$] $\oplus$ [$n = 1$] $\oplus$ [$n = 2$] space by using the boson m scheme [60]. The resulting wave function is then used to compute the electromagnetic $E2$ transition rates. The $E2$ transition operator is given as

$$\hat{T}^{(E2)} = \sum_{n=0,1,2} e_{B,n} \hat{Q}_n, \qquad (12)$$

where $e_{B,n}$ and $\hat{Q}_n$ are the effective charge and quadrupole operator for the configuration [n], respectively. For simplicity, the effective charges are assumed to be the same for the three configurations, i.e., $e_{B,n=0} = e_{B,n=1} = e_{B,n=2}$. They are fit to reproduce the available experimental $B(E2; 2_1^+ \rightarrow 0_1^+)$ values for the $N = 66$ Ru, Mo, and Zr nuclei while for the Sr isotopes they are fit to reproduce the experimental $B(E2; 2_1^+ \rightarrow 0_1^+)$ value for ^{100}Sr.

III. RESULTS AND DISCUSSION

A. The Gogny-D1M energy surfaces

In this section, we discuss the results of our SCMF calculations. In Figs. 1 and 2 we depict the deformation-energy surfaces, obtained within the constrained Gogny-D1M EDF framework, for the considered Ru, Mo, Zr, and Sr even-even nuclei with neutron numbers $54 \leqslant N \leqslant 70$.

As can be seen from Fig. 1, the lightest of the considered Ru isotopes exhibits a weakly deformed minimum. On the other hand, for $N = 60$ the ground state corresponds to a shallow triaxial configuration around $\gamma = 30°$. In fact, the nucleus ^{104}Ru is the softest in the γ direction among all the

Ru isotopes shown in the figure. Moreover, the ground-state minimum remains triaxial up to $N = 68$. For larger neutron numbers, the ground state becomes oblate although it still remains γ soft. For the studied Ru nuclei, the mean-field energy surfaces do not display multiple minima.

In the case of the Mo isotopes, also shown in Fig. 1, the energy surface corresponding to ^{96}Mo displays a nearly spherical minimum while for increasing neutron number the surfaces become γ soft up to $N = 62$. Previous Skyrme Hartree–Fock plus BCS calculations [5], based on the SLy6 parameter set [61], predicted two minima: one nearly spherical and the other triaxial, for ^{98}Mo. On the other hand, in our Gogny-D1M SCMF calculations no coexisting minima are found for ^{98}Mo, as well as for ^{100,102}Mo. Two minima are found in the SCMF energy surfaces from around $N = 62$, one oblate and the other triaxial with γ around $20°–30°$. However, the heavier isotopes are less γ soft with coexisting oblate and nearly spherical configurations in the case of ^{112}Mo.

The systematics of the HFB energy surfaces, depicted in Fig. 2 for the Zr and Sr isotopes, reveals a pronounced competition between oblate and prolate configurations. In the case of Zr nuclei, the oblate minimum remains the ground state up to ^{100}Zr. The two mean-field minima found for $N = 62$ and 64 are quite close in energy whereas the global minimum is still found on the oblate side. For $N \geqslant 66$, the prolate minimum becomes less pronounced. For the Sr isotopes, a clear prolate minimum is found for $N = 60, 62$, and 64. The energy surfaces obtained for ^{104,106}Sr display two almost degenerate minima while the oblate one becomes more pronounced for ^{108}Sr. The previous results agree well with those obtained with the Gogny-D1S EDF [12,62]. For $N \approx 60$ isotones, the constrained Hartree–Fock plus BCS calculations, based on the Skyrme SLy4 [63] parameter set, predicted a trend similar to ours, i.e., an oblate-to-prolate shape transition between $N = 58$ and 60. A more gradual transition has been found within the relativistic mean-field framework based on the PC-PK1 parametrization and a density-dependent pairing [14]. For both Zr and Sr nuclei, an oblate (prolate) ground-state minimum has been found for $N = 58$ ($N = 60$) in the framework of the Nilsson–Strutinsky method with a deformed Woods–Saxon potential and monopole pairing [20].

B. Choice of interacting boson model configuration spaces

We have performed the configuration-mixing calculations in many of the nuclei considered, where multiple mean-field minima have been observed in the corresponding Gogny-D1M energy surfaces. The criterion for choosing configuration spaces is whether a mean-field minimum is clear (or deep) enough to constrain the corresponding unperturbed Hamiltonian. Using this criterion, configuration-mixing calculations have been carried out for heavier Mo nuclei and most of the Zr and Sr nuclei. However, such calculations have not been carried out for all the Ru isotopes and the lightest nuclei in other isotopic chains, since the microscopic Gogny-D1M energy surfaces only show one clear minimum (see Figs. 1 and 2).
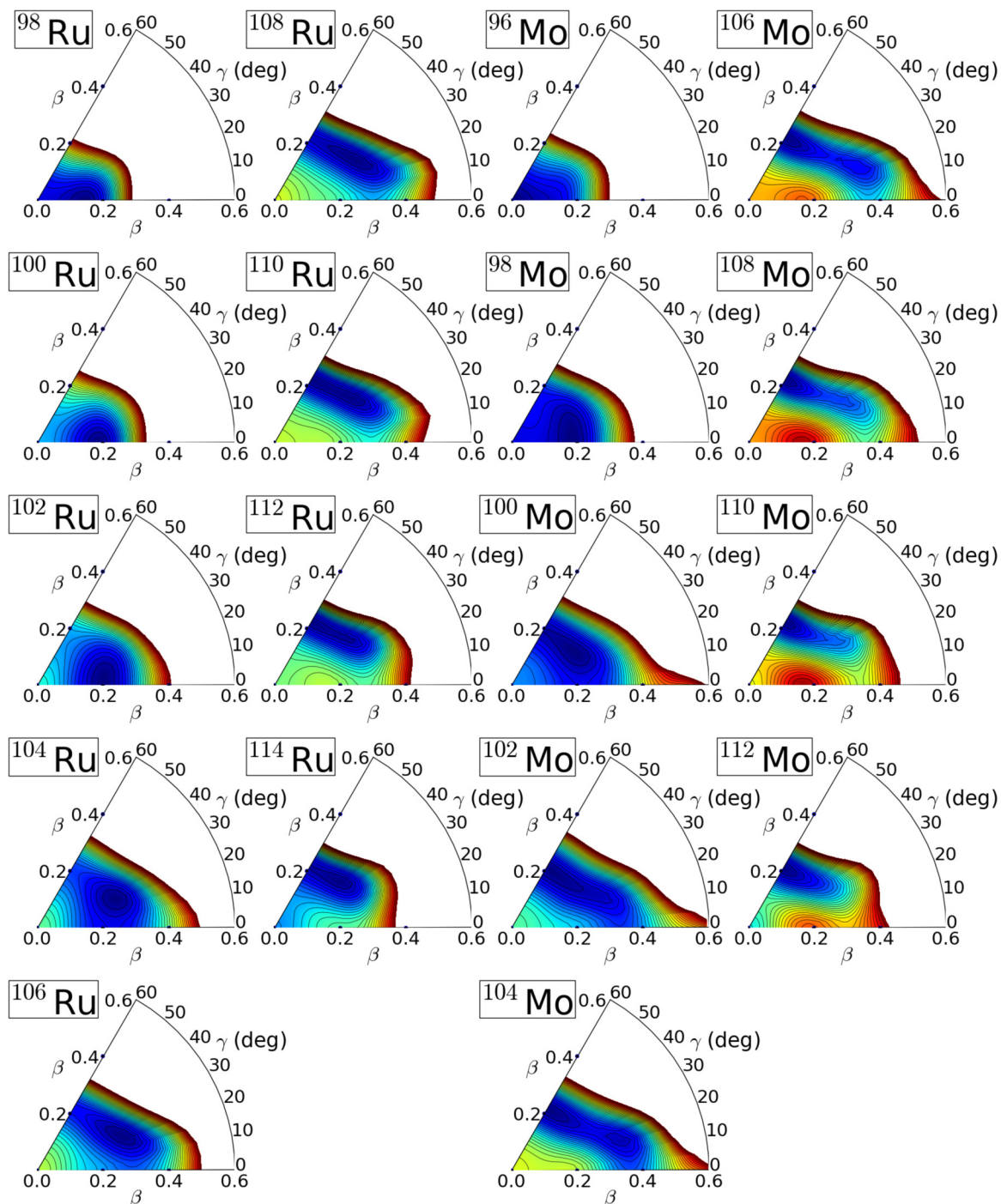
FIG. 1. Contour plot of the deformation-energy surfaces in the (β, γ) plane for the considered Ru and Mo isotopes from neutron number $N = 54$ to 70, computed with the constrained HFB method by using the Gogny functional D1M. They are plotted in the range $0.0 \leqslant \beta \leqslant 0.6$ and $0° \leqslant \gamma \leqslant 60°$. The difference between the neighboring contours is 100 keV.

For the sake of clarity, in what follows we summarize the configuration spaces for the nuclei considered in this work:

(i) Ru: normal $[N_\nu \otimes (N_\pi = 2)]$ configuration for all isotopes.

(ii) Mo: normal $[N_\nu \otimes (N_\pi = 1)]$ configuration for $^{96-102}$Mo, and $[N_\nu \otimes (N_\pi = 1)] \oplus [N_\nu \otimes (N_\pi = 3)]$ configuration for $^{104-112}$Mo.

(iii) Zr: normal $[N_\nu \otimes (N_\pi = 0)]$ configuration for ^{94}Zr, $[N_\nu \otimes (N_\pi = 0)] \oplus [N_\nu \otimes (N_\pi = 2)]$ configuration for ^{96}Zr, and $[N_\nu \otimes (N_\pi = 0)] \oplus [N_\nu \otimes (N_\pi = 2)] \oplus [N_\nu \otimes (N_\pi = 4)]$ configuration for $^{98-110}$Zr.

(iv) Sr: normal $[N_\nu \otimes (N_\pi = 1)]$ configuration for $^{92-94}$Sr, $[N_\nu \otimes (N_\pi = 1)] \oplus [N_\nu \otimes (N_\pi = 3)]$ configuration for ^{96}Sr, and $[N_\nu \otimes (N_\pi = 1)] \oplus [N_\nu \otimes (N_\pi = 3)] \oplus [N_\nu \otimes (N_\pi = 5)]$ configuration for $^{98-108}$Sr.
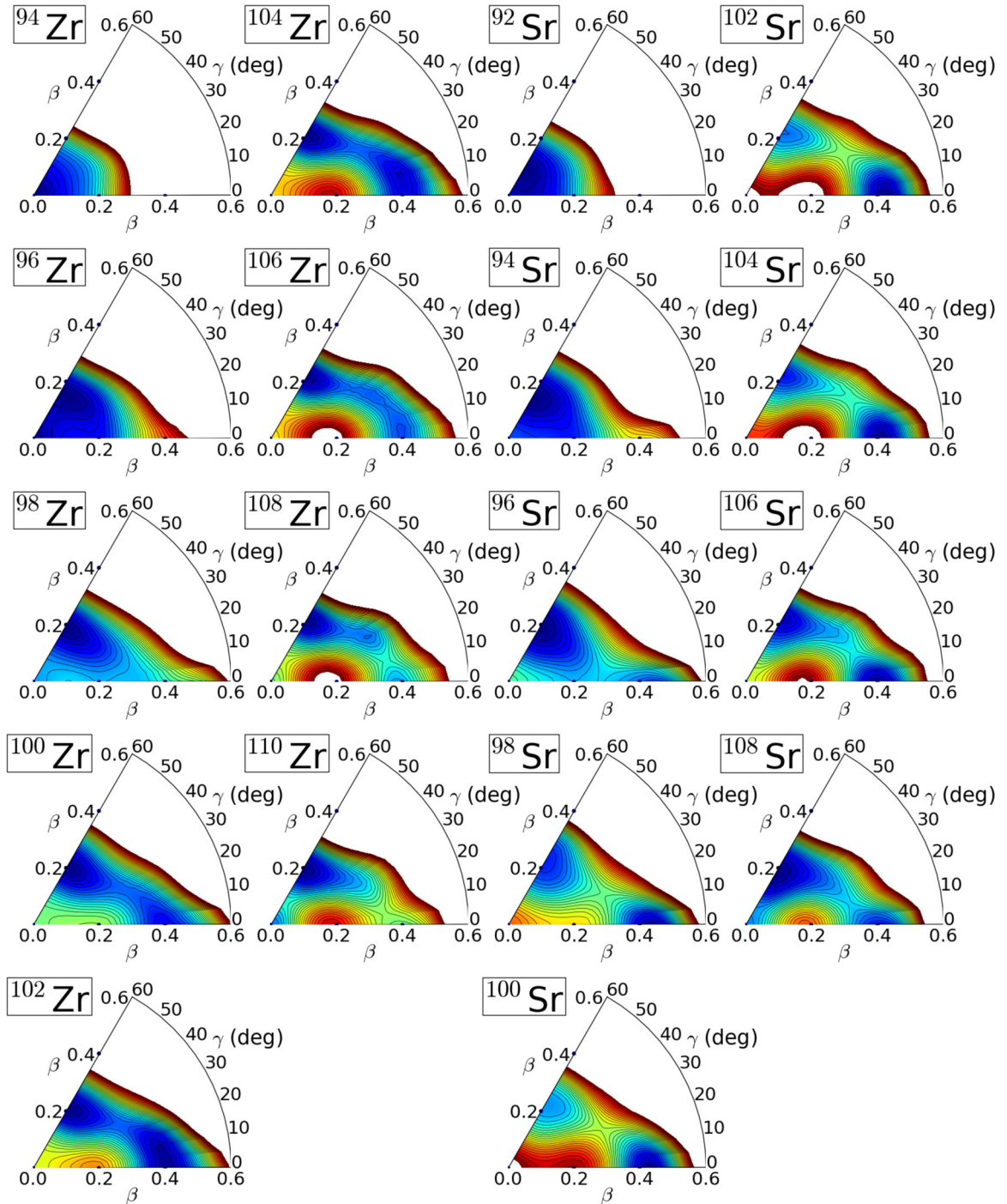
FIG. 2. The same as in Fig. 1, but for the Zr and Sr isotopes.

In Fig. 3 the HFB energies of $^{104-112}$Mo, $^{96-110}$Zr, and $^{96-108}$Sr are plotted as a function of the β deformation parameter. These are the nuclei where configuration mixing is taken into account in the corresponding IBM space. The β coordinates associated with the [n] ($n = 0$, 1, and 2) spaces are indicated in the plots. In Fig. 3(b), we consider ^{100}Zr as an illustrative example. In this case, the global minimum is oblate with $\beta \approx -0.2$ and is associated with the [$n = 1$] configuration. The second-lowest minimum on the prolate side is associated with the [$n = 2$] configuration and, finally, the third, almost spherical, minimum is associated with the normal [$n = 0$] configuration. Within our framework, the ground state 0_1^+ is mainly composed of the configuration associated with the global minimum, while the 0_2^+ excited state is constructed mainly from the configuration associated with the second-lowest minimum. In the particular example of ^{100}Zr, as shown later in Fig. 13, the 0_1^+ (0_2^+) state is predominantly composed of the oblate (prolate) configuration.
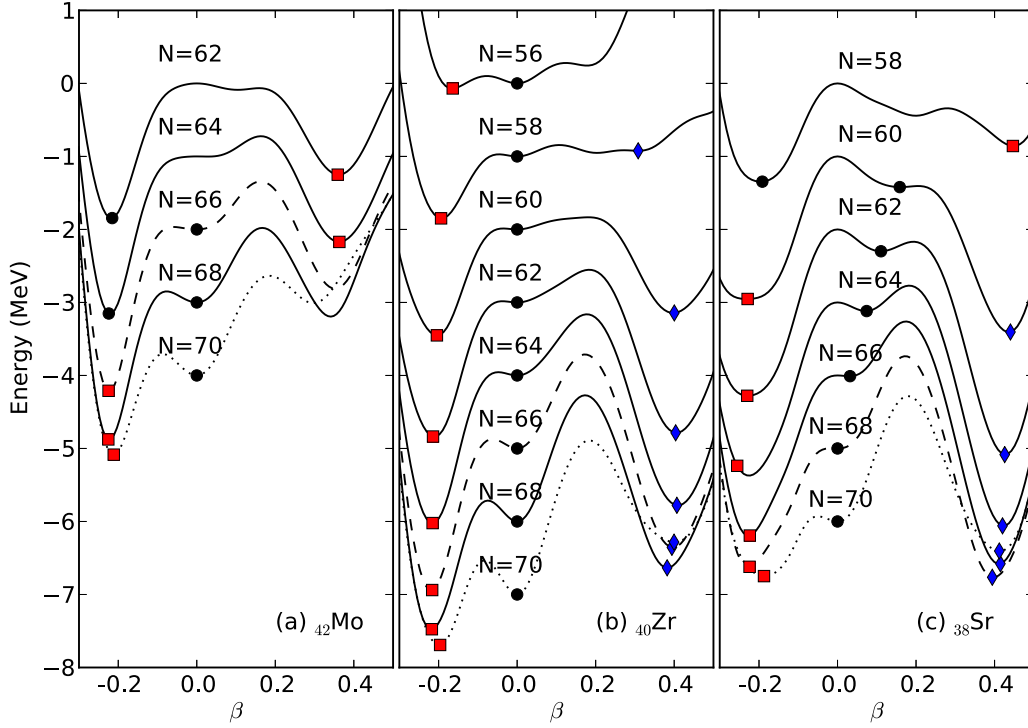
FIG. 3. Projection of the HFB deformation-energy surfaces along the β axis for (a) $^{106-112}$Mo, (b) $^{96-110}$Zr, and (c) $^{96-108}$Sr isotopes, where configuration mixing is taken into account in the corresponding IBM space. Solid circles, squares, and diamonds represent the β values associated with the $[n]$ ($n = 0$, 1, and 2) unperturbed Hamiltonians, respectively.

C. Mapped interacting boson model deformation-energy surface

In Figs. 4 and 5, we plot the IBM energy surfaces corresponding to the Hamiltonian (2), whose parameters have been determined by mapping the Gogny-D1M energy surfaces shown in Figs. 1 and 2.

Similar to the SCMF case, one observes for the Ru nuclei, shown in Fig. 4, an evolution of the ground-state deformation from nearly spherical to triaxial for ^{104}Ru. The absolute minimum of the IBM surfaces becomes oblate for larger neutron numbers. The mapped surfaces obtained for Mo isotopes exhibit sharper minima than those found at the mean-field level. Moreover, for the neutron number $N \geqslant 66$ the mapped IBM surface is less γ soft than the mean-field one. The IBM surfaces for Zr and Sr nuclei in Fig. 5 also reproduce the overall HFB trend as a function of the neutron number. In particular, they account for the onset of the strongly deformed prolate shape around $N = 60$ as well as a pronounced competition between the prolate and oblate minima for $60 \leqslant N \leqslant 64$ in the case of Zr and $58 \leqslant N \leqslant 70$ for Sr nuclei.

As can be seen, the mapped energy surfaces reproduce the basic features of the mean-field ones. However, some discrepancies remain as the topology of the SCMF energy surfaces is richer than the IBM one. In particular, the mapped IBM surfaces tend to become flat in the region far from the minimum. There are essentially two reasons for this behavior: first, the analytical expressions of Eqs. (9) and (11) are too restricted to reproduce every detail of the original HFB energy surfaces and, second, that the number and/or kind of

bosons are rather limited within our IBM framework. One also observes substantial differences in the barriers between the different minima. This is partly due to the adopted mixing strength value $\omega = 0.1$ MeV that may not be a proper choice for fully reproducing the barriers. The employed value $\omega = 0.1$ MeV is a guess based on our experience from previous calculations [35,36]. However, as will be shown later, it leads to a reasonable description of spectroscopic properties. To fully reproduce the barriers, a much larger ω value would be necessary. However, the larger ω value implies the stronger level repulsion between the states and the model description would become unrealistically worse. For this reason, and since we are rather interested in describing an overall systematic trend of the spectroscopic properties, we have tried not to reproduce full details of the barriers and used a realistic mixing strength $\omega = 0.1$ MeV.

Once the parameters of the Hamiltonian in Eq. (2) have been fixed by the mapping procedure described in Sec. II, spectroscopic calculations are carried out to obtain excitation energies and transition probabilities.

D. Parameters

The parameters employed in our calculations for Ru, Mo, Zr, and Sr isotopes are displayed in Figs. 6–10. They are obtained as a result of the mapping procedure and their variations, as functions of neutron number, reflect structural changes along the considered isotopic chains. We have not plotted the values of the strength κ' associated with the three-boson term because, in most of the cases, it is the same
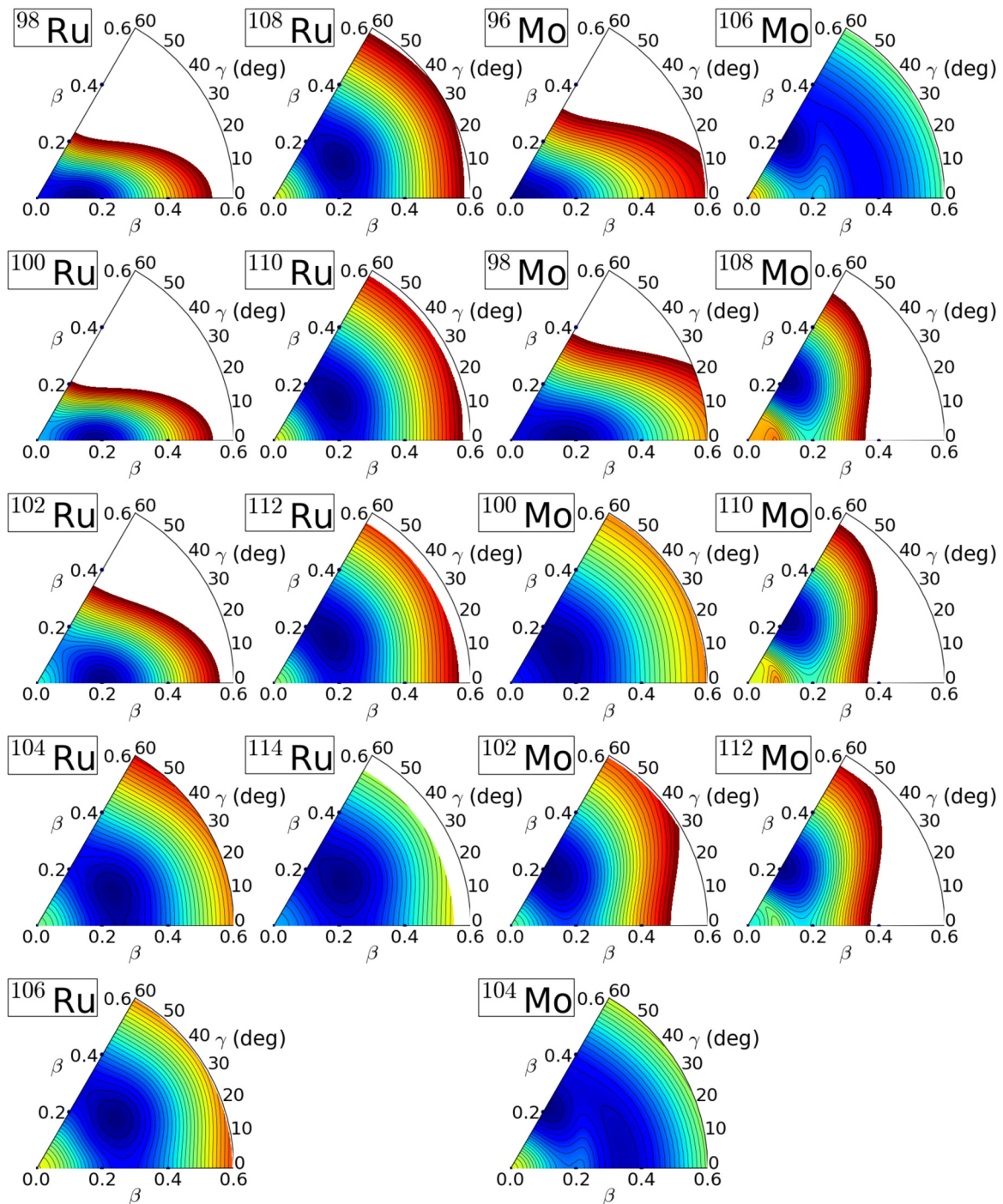
FIG. 4. The same as in Fig. 1, but for the mapped IBM and for the Ru and Mo isotopes.

as the strength κ for the quadrupole-quadrupole interaction. The exceptions are $^{104-114}$Ru and $^{100-102}$Mo. Their κ' values are 0.25, 0.25, 0.12, 0.08, 0.10, and 0.18 MeV for $^{104-114}$Ru and the constant value 0.50 MeV for $^{100-102}$Mo.

In Figs. 6(a) and 6(b), we plot the parameter ϵ for Ru and Mo nuclei, respectively. For most of the nuclei only a single configuration has been used in the calculations. As can be seen, ϵ decreases gradually towards the middle of the major shell. For the Mo isotopes, the value of ϵ for the normal configuration exhibits a jump between $N = 64$ and $N = 66$.

This is so because the structure of the unperturbed Hamiltonian for the normal configuration changes from $N = 64$ to 66: the normal configuration is associated with the oblate minimum for $N \leqslant 64$, whereas it is associated with the nearly spherical minimum for $N \geqslant 66$ (see Fig. 1).

For the Zr nuclei, shown in Fig. 6(c), ϵ decreases in heavier isotopes. However, the ϵ values for the $[n = 1]$ and $[n = 2]$ configurations change little for $N \geqslant 60$. For the Sr isotopes, shown in Fig. 6(d), except for the jump from $N = 58$ to 60, an almost constant value is obtained. The
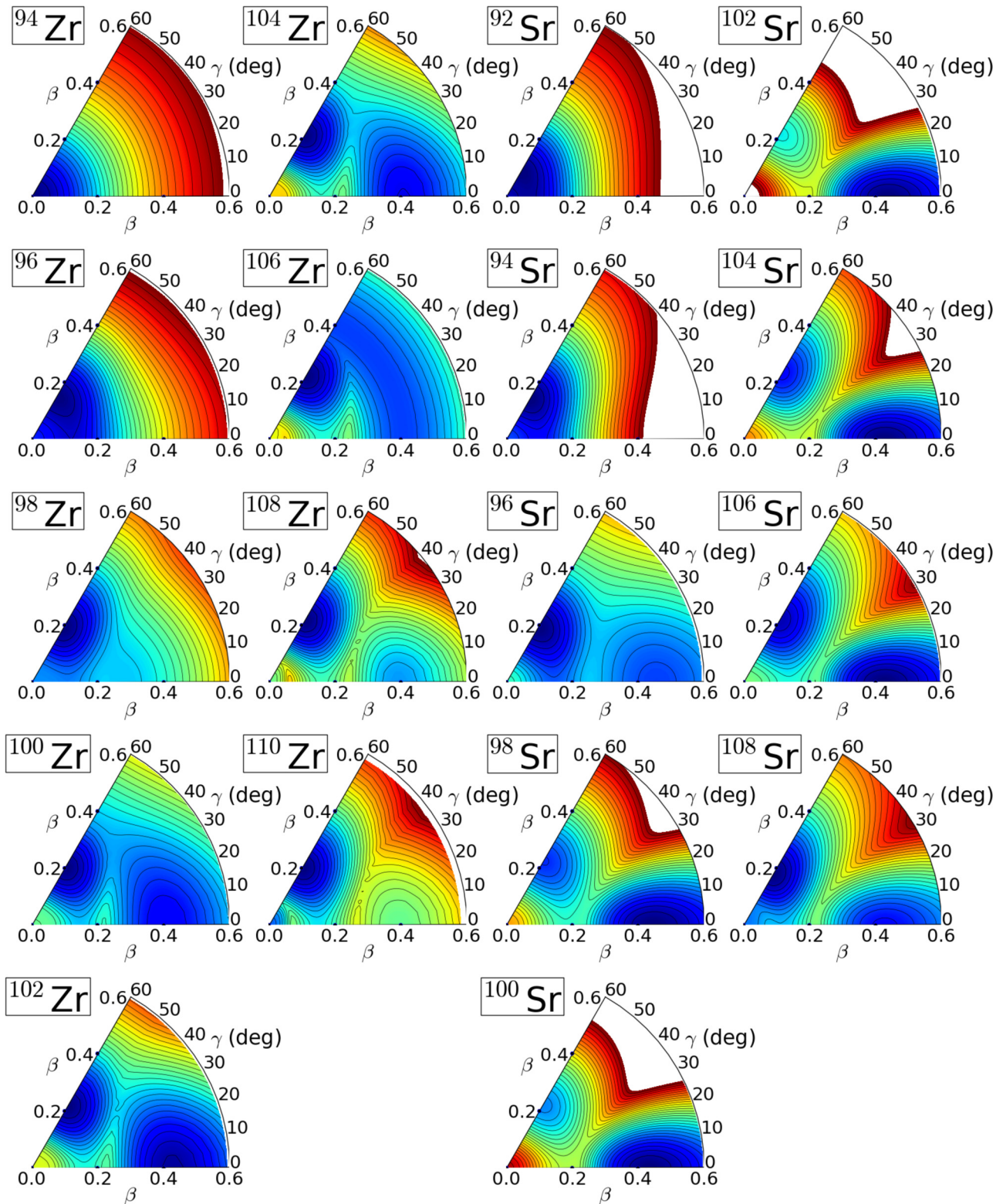
FIG. 5. The same as in Fig. 1, but for the mapped IBM and for the Zr and Sr isotopes.

parameter κ, plotted in Figs. 7(a)–7(d), exhibits a gradual decrease towards the midshell for all configurations, which is consistent with the general mass-number dependence of this parameter [30,53,55].

The parameters χ_ν and χ_π are depicted in Figs. 8 and 9. A certain combination of those parameters reflects whether a nucleus is either prolate or oblate deformed. From Eqs. (3), (9), and (10), one sees that the γ dependence of the unperturbed
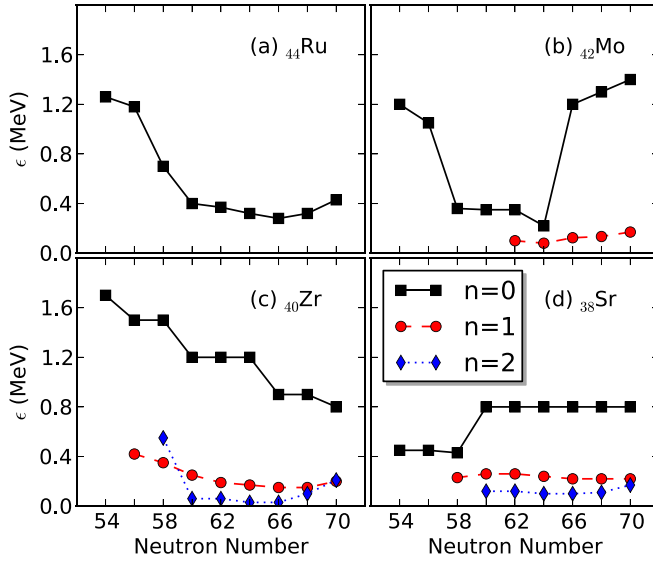
FIG. 6. The parameter ϵ (in MeV) for the unperturbed configuration spaces $[n]$ ($n = 0, 1,$ and 2) is plotted as a function of neutron number for the considered Ru, Mo, Zr, and Sr isotopes.

FIG. 8. The same as in Fig. 6, but for the parameter χ_ν (dimensionless).

Hamiltonian is associated with the two terms proportional to $-\kappa(N_\nu\chi_\nu + N_\pi\chi_\pi)\cos 3\gamma$ in the quadrupole-quadrupole interaction $\hat{Q} \cdot \hat{Q}$ and $-\kappa'\sin^2 3\gamma$ in the three-boson term. Since the $\hat{Q} \cdot \hat{Q}$ is attractive ($\kappa < 0$) then the minimum turns out to be prolate (oblate) if $N_\nu\chi_\nu + N_\pi\chi_\pi < 0$ ($N_\nu\chi_\nu + N_\pi\chi_\pi > 0$). The three-boson term becomes important only when the nucleus is γ soft, i.e., $N_\nu\chi_\nu + N_\pi\chi_\pi \approx 0$. The development of a triaxial minimum then depends on the strength of the three-boson interaction (κ'). For many of the Ru and Mo nuclei, both χ_ν and χ_π are close to zero for $N \geqslant 60$ [see panels (a) and (b) of Figs. 8 and 9] and the corresponding κ' values are large enough to produce a triaxial minimum. The energy surfaces for many of the heavier Ru and Mo isotopes (see Figs. 1 and 4) display shallow
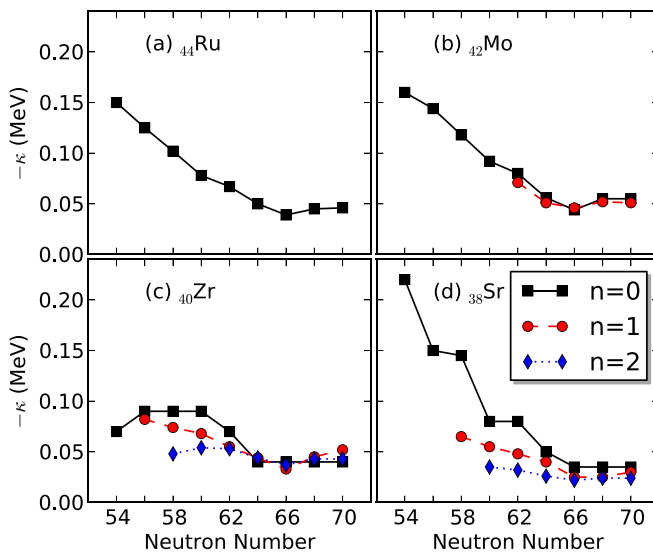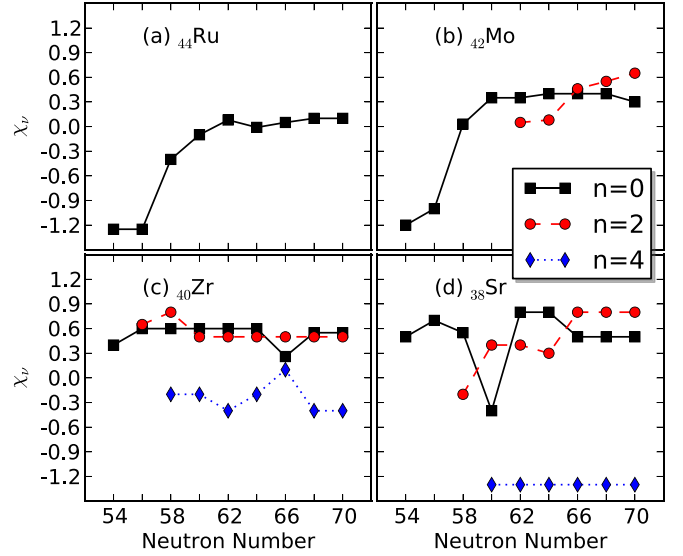
triaxial minima. From panels (c) and (d) of Figs. 8 and 9, the χ_ν and χ_π values for most of the Zr and Sr isotopes are chosen so as not to change too much with neutron number. Many of the deformation-energy surfaces for the Sr isotopes exhibit pronounced prolate minimum around $\beta = 0.4$, which are associated with the $[n = 2]$ configuration. Consequently, their χ_ν and χ_π values for the $[n = 2]$ configuration are notably large ≈ -1.3, being close to the SU(3) limit of the IBM.

The offset energies Δ_1 and Δ_2 used in our configuration-mixing calculations are shown in Fig. 10. They are of the order of a few MeV. This is consistent with the results of previous studies [35,36] in different regions of the nuclear chart.
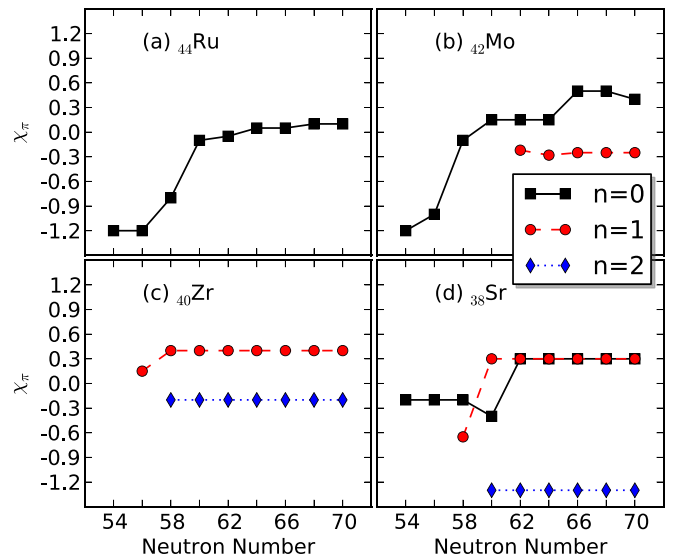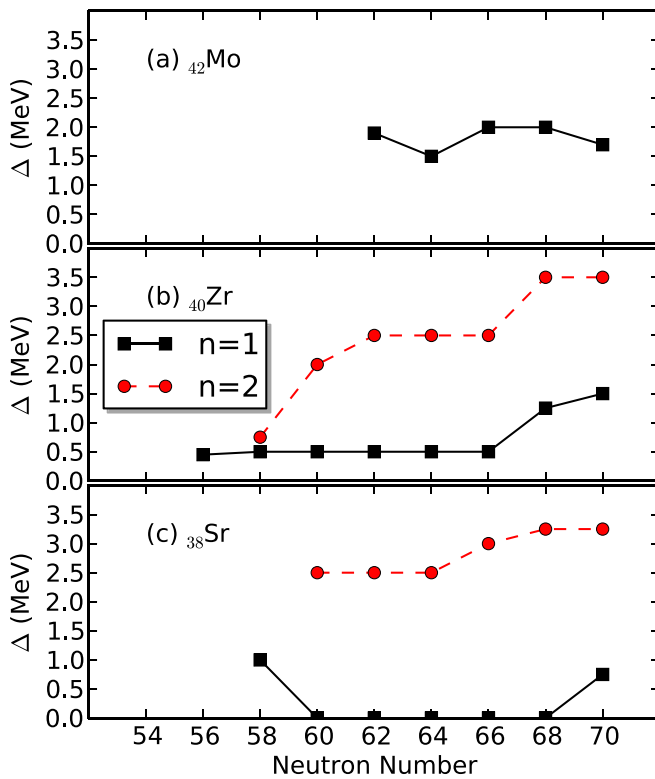

FIG. 7. The same as in Fig. 6, but for the parameter κ (in MeV).

FIG. 9. The same as in Fig. 6, but for the parameter χ_π (dimensionless).

FIG. 10. The energy offsets Δ_1 and Δ_2 (in MeV) are plotted as a function of neutron number for the Mo, Zr, and Sr isotopes.

However, we have chosen $\Delta_2 = 0$ for the Sr isotopes with $60 \leqslant N \leqslant 68$ [see Fig. 10(c)], due to the peculiar topology of the corresponding HFB surfaces.

E. Evolution of low-lying levels

The energies of some low-lying yrast and nonyrast states in $^{98-114}$Ru, $^{96-112}$Mo, $^{94-110}$Zr, and $^{92-108}$Sr are shown in Figs. 11 and 12 as functions of neutron number N. The energies of the yrast states decrease towards $N = 66$, corresponding to midshell. They remain quite low for heavier Zr and Sr nuclei, reflecting a pronounced collectivity. Experimentally, an abrupt change is observed in going from $N = 58$ to 60 in the Zr and Sr chains. Although our calculations account reasonably well for the experimental trend in the low-energy yrast states, in particular for the heavier ($N \geqslant 60$) isotopes, several deviations are also found:

(i) The energy levels near the neutron shell closure $N = 50$ are overestimated. This is due to the fact that the IBM model space, comprising only a finite number of s and d bosons, is not large enough to describe the energy levels near the closed shell.

(ii) For Zr isotopes, the present calculation predicts that the yrast states change from $N = 58$ to 60 gradually, whereas a much more drastic change is observed experimentally. This indicates that, in the present model calculation, these yrast states are rather similar in structure between the ^{98}Zr and ^{100}Zr nuclei. In both nuclei, the yrast states are mainly composed of the oblate [$n = 1$] configuration. Note that the topology of the Gogny-D1M energy surface around this oblate minimum is rather similar for the two nuclei.

(iii) In the case of the Zr isotopes, the experimental high-lying yrast levels at $N = 56$ suggest the presence of a subshell closure. In our calculations, however, such a feature is not reproduced. This is not surprising, since the present IBM model space does not consider
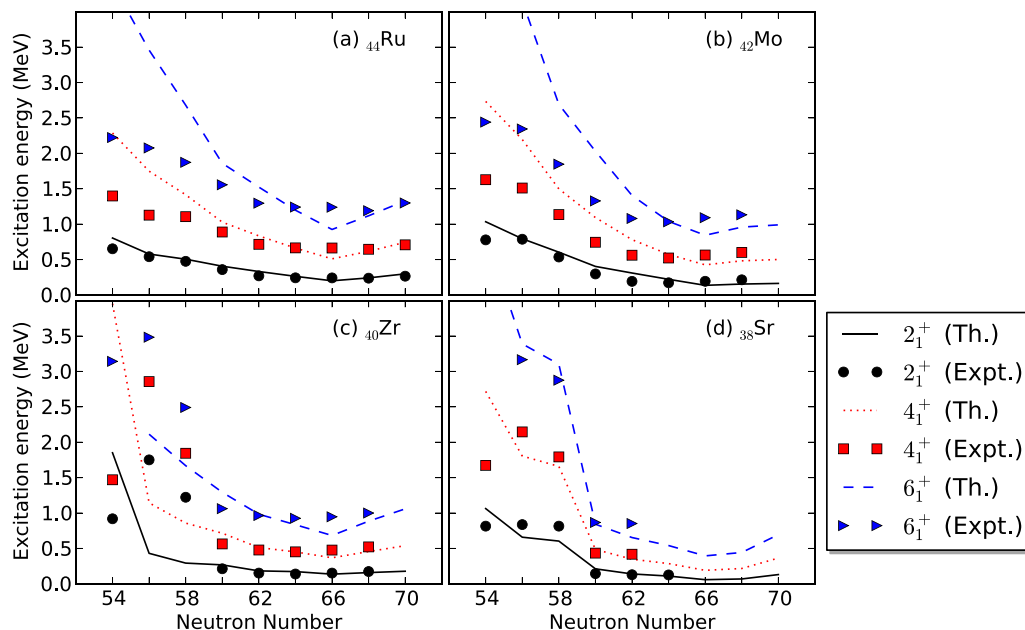

FIG. 11. Evolution of the low-lying yrast states in the considered Ru, Mo, Zr, and Sr isotopes as a function of the neutron number. Experimental data have been taken from Ref. [64].
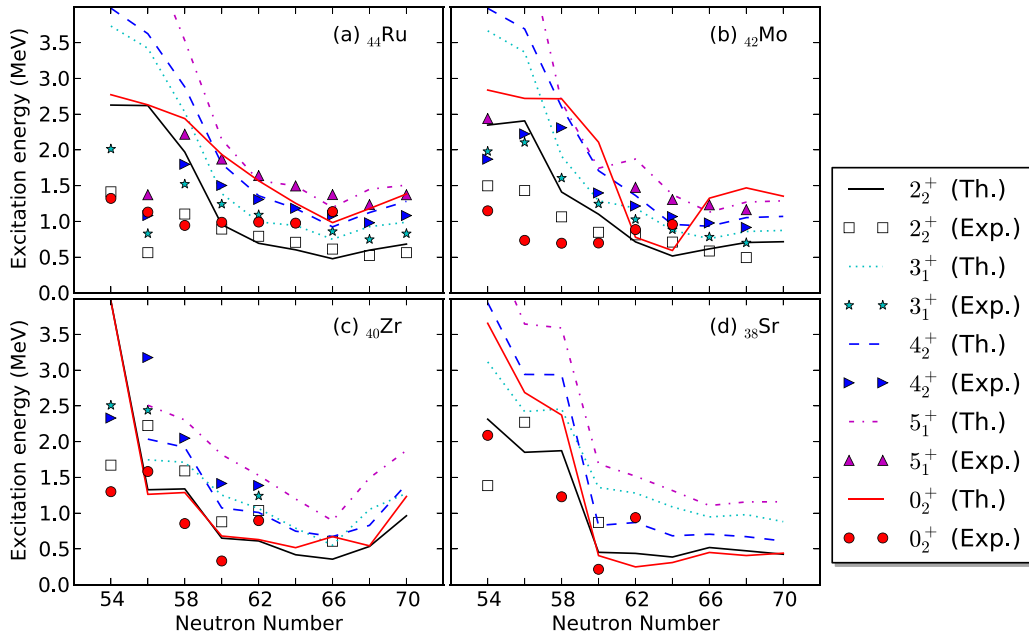
FIG. 12. The same as in Fig. 11, but for the nonyrast states.

$N = 56$ to be a shell closure and, as a consequence, the energy levels change rather gradually from $N = 54$ to 56, as already found in previous IBM calculations [11].

From the systematics of the nonyrast states depicted in Fig. 12, one sees a typical γ-band sequence $2^+, 3^+, 4^+, 5^+, \ldots$. The deviation with respect to the experimental data near

$N = 50$ could also be due to the limited number and/or types of bosons taken into account in our calculations. For both the Ru and Mo nuclei, the excitation energy of the 0_2^+ state is generally overestimated because the intruder configuration is not considered in many of these nuclei, since the Gogny-HFB energy surface does not exhibit coexisting minima (see Fig. 1). The 0_2^+ energy level for the $N = 62$ and 64 Mo nuclei is mostly
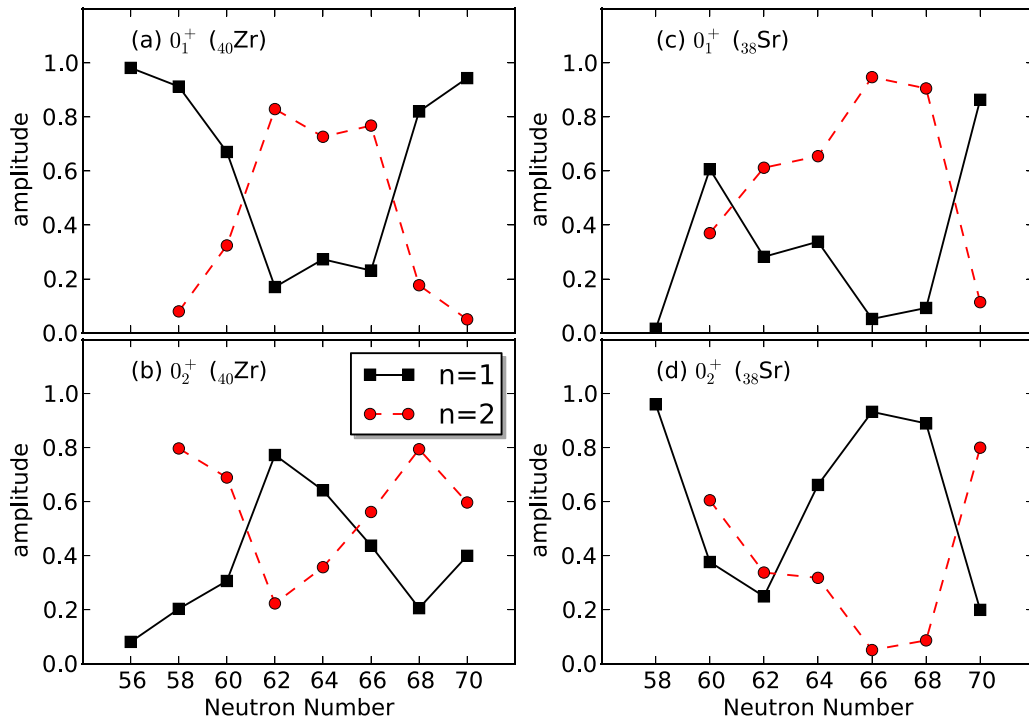

FIG. 13. Amplitudes of the unperturbed $[n = 1]$ and $[n = 2]$ components in the wave functions of the 0_1^+ and 0_2^+ states of $^{96-110}$Zr [panels (a) and (b)] and $^{96-108}$Sr [panels (c) and (d)] isotopes.

coming from the γ-soft minimum on the prolate side close in energy to the oblate global minimum (see Fig. 4) and is, consequently, notably low compared with other Mo nuclei.

For the nucleus ^{98}Mo, already described by using configuration-mixing IBM calculations in Refs. [5,39], we obtained a pronounced deviation of the 0_2^+ excitation energy with respect to the experimental value. Note that, at variance with previous results [5], our calculations on the deformation-energy surfaces with the Gogny-D1M EDF (see Fig. 1) predict a single minimum around $\beta \approx 0.15$ (see Fig. 1). The structure of the Zr and Sr isotopes is characterized by very-low-lying excited 0^+ states. In our calculations, the excited 0^+ states are mainly dominated by the intruder configurations and their energies are similar to the energy difference between different mean-field minima. Our results suggest that, for the Zr and Sr isotopes, the 0_2^+ excitation energy decreases from $N = 58$ to $N = 60$. This reflects the fact that, in the mean-field calculations, the second prolate minimum appears from $N = 60$. On the other hand, the experimental 0_2^+ excitation energy increases from $N = 60$ to 62 while in our calculations it remains low.

F. Wave functions for 0_1^+ and 0_2^+ states

To interpret the nature of the lowest two 0^+ states, we plot in Fig. 13 the amplitudes of the unperturbed $[n = 1]$ and $[n = 2]$ components in the wave functions of the 0_1^+ and 0_2^+ states for the Zr and Sr nuclei. In most of the cases, the wave functions are composed predominantly of the oblate $[n = 1]$ and prolate $[n = 2]$ configurations, while the contribution of the normal $[n = 0]$ configuration turns out to be negligible. For this reason, we do not show the amplitude of the normal $[n = 0]$ configuration. One should keep in mind that for ^{96}Zr

FIG. 15. The same as in Fig. 14, but for the $B(E2; 4_1^+ \rightarrow 2_1^+)$ transition strength. Data have been taken from Ref. [64].

and ^{96}Sr, the $[n = 2]$ configuration is not included. So the 0_1^+ (0_2^+) state of ^{96}Zr (^{96}Sr) is almost purely made of the oblate (prolate) normal ($[n = 1]$) configuration.

From Fig. 13, one sees some characteristic features in the contents of the 0_1^+ and 0_2^+ wave functions for $^{98-110}$Zr and $^{98-108}$Sr isotopes. From Fig. 13(a), one realizes that the 0_1^+ state for ^{98,100}Zr is dominated by the oblate configuration. For $N = 62-66$, on the contrary, the 0_1^+ wave function is
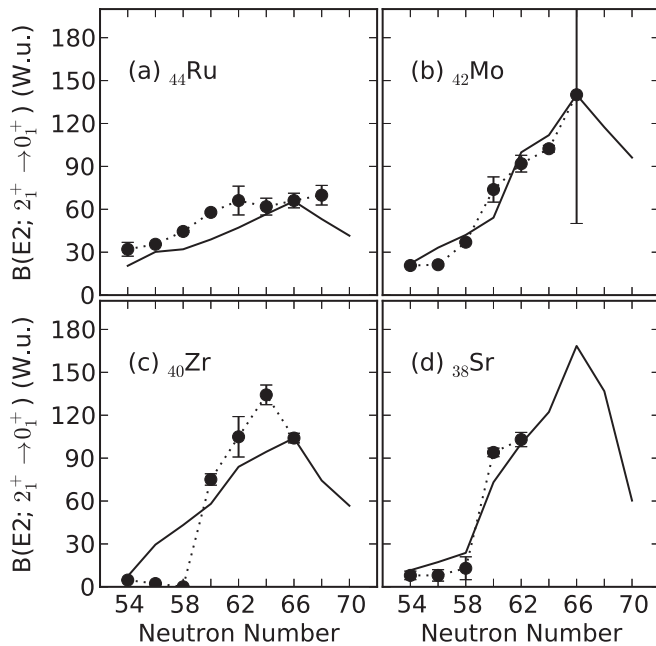

FIG. 14. $B(E2; 2_1^+ \rightarrow 0_1^+)$ transition strength (in Weisskopf units) for the considered Ru, Mo, Zr and Sr isotopes as a function of the neutron number. Data have been taken from Refs. [6,64].
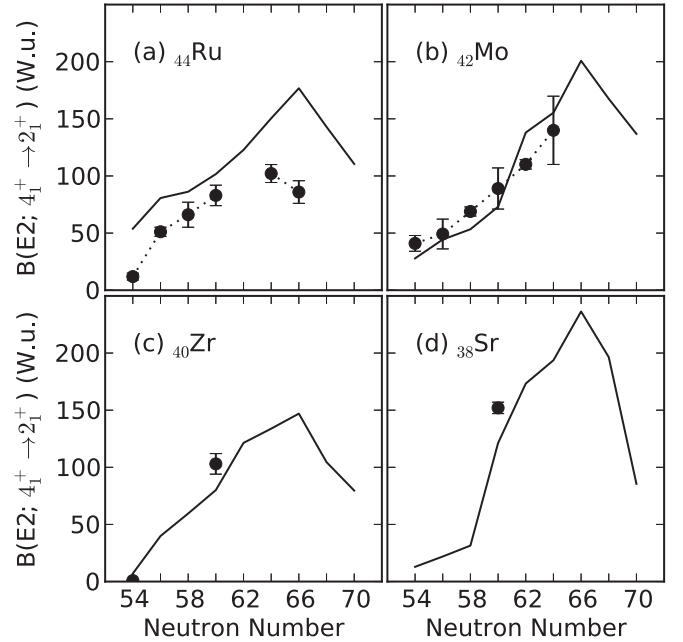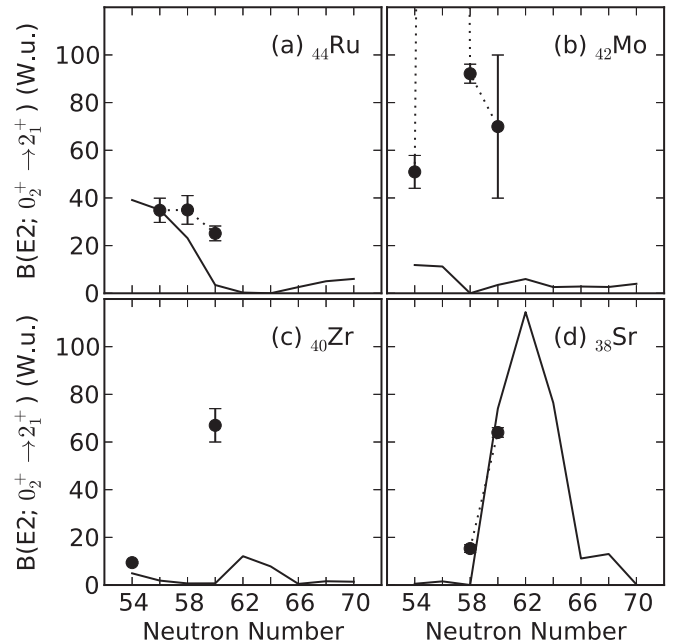

FIG. 16. The same as in Fig. 14, but for the $B(E2; 0_2^+ \rightarrow 2_1^+)$ transition strength. Data have been taken from Ref. [64].
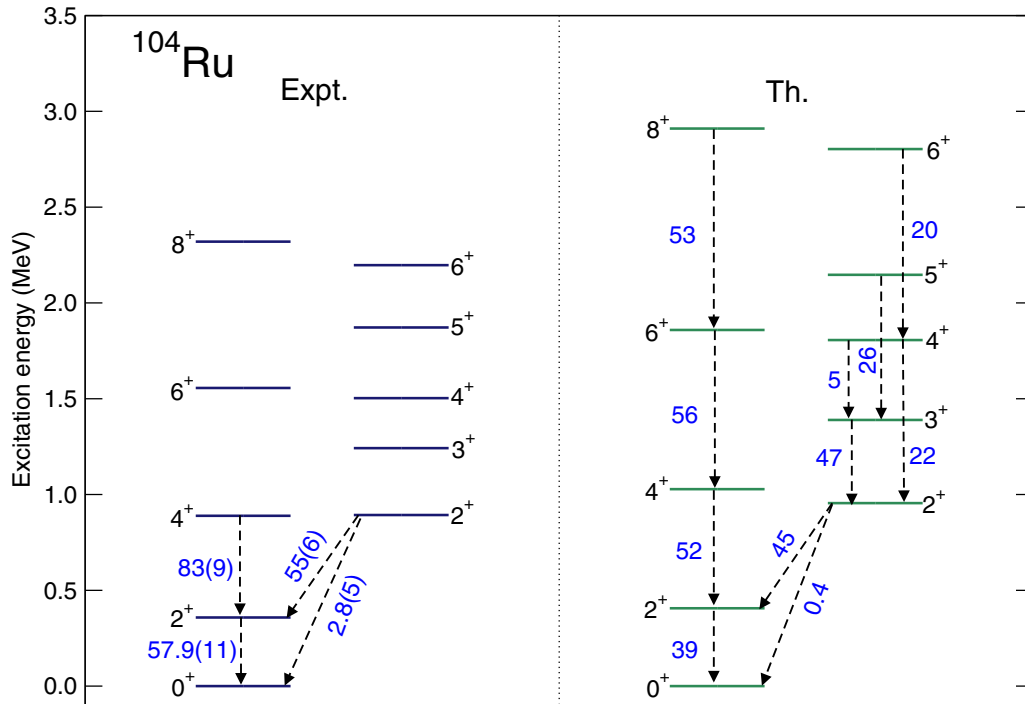
FIG. 17. Low-energy-level scheme for ^{104}Ru. The numbers (in blue) near the arrows stand for the $B(E2)$ values in Weisskopf units. Experimental data have been taken from Ref. [64].

predominantly prolate while, for the $N = 68$ and 70 isotopes, the oblate configuration becomes dominant again. On the other hand, the systematics of the 0_2^+ states, shown in Fig. 13(b) of the figure, reveals that the prolate configuration is dominant for $N = 58$ and 60, the oblate configuration makes a major

contribution for $N = 62$ and 64 while the prolate configuration again dominates for $N = 68$ and 70. Similar results are found for the 0^+ states in the Sr chain but more isotopes are found for which the prolate configuration becomes dominant in the ground state. The previous results are basically consistent
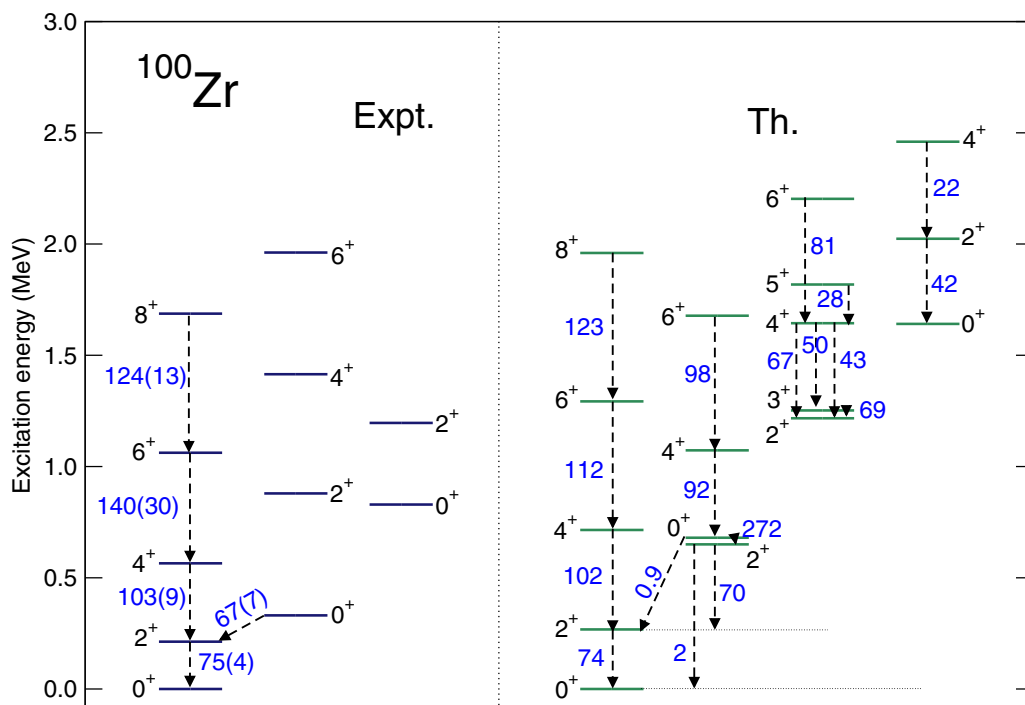

FIG. 18. The same as in Fig. 17, but for the ^{100}Zr nucleus. Data have been taken from Ref. [64].

with those obtained at the HFB level (see Figs. 2 and 5), i.e., an oblate ground state is observed for the isotopes with neutron numbers below $N \approx 58$ and beyond $N \approx 68$, and a pronounced competition between an oblate and a prolate minima in between.

G. $B(E2)$ systematics

Figures 14–16 show the $B(E2)$ transition strengths between the low-spin states, $B(E2; 2_1^+ \rightarrow 0_1^+)$, $B(E2; 4_1^+ \rightarrow 2_1^+)$, and $B(E2; 0_2^+ \rightarrow 2_1^+)$, respectively. The in-band $B(E2; 2_1^+ \rightarrow 0_1^+)$ and $B(E2; 4_1^+ \rightarrow 2_1^+)$ transitions become maximal around the neutron number $N = 66$ corresponding to midshell where the largest quadrupole collectivity is expected. In the case of the Zr isotopes, the experimental systematics suggests that the $B(E2; 2_1^+ \rightarrow 0_1^+)$ transition strength remains small for $N = 56$ and 58 (Fig. 14) while ours increases gradually due to the fact that, in the IBM model space considered, the $N = 56$ subshell closure is not taken into account.

The interband $B(E2; 0_2^+ \rightarrow 2_1^+)$ transition is shown in Fig. 16. Near the vibrational limit, the value is comparable in magnitude to the $B(E2; 2_1^+ \rightarrow 0_1^+)$ magnitude. However, it becomes small in the deformed limit where such a transition is not allowed. Within this context, a vibrational-like behavior is suggested for the lighter Ru isotopes for which the deformation of the minimum in the corresponding mean-field-energy surfaces is small. For heavier isotopes, this transition becomes small as the deformation becomes stronger.

For Mo isotopes, the quite large experimental $B(E2; 0_2^+ \rightarrow 2_1^+)$ value of 1400 ± 200 W.u. [5] [not shown in Fig. 16(b)] suggests a large mixing between the different intrinsic structures while the theoretical value is much smaller. The reason for the discrepancy is that for the lighter Mo nuclei configuration mixing is not taken into account in our calculations. A similar observation applies to Zr and Sr isotopes. For the former, the coupling between the 0_2^+ and 2_1^+ states is probably not strong enough to reproduce the experimental data while for the latter the trend is reasonably well described.
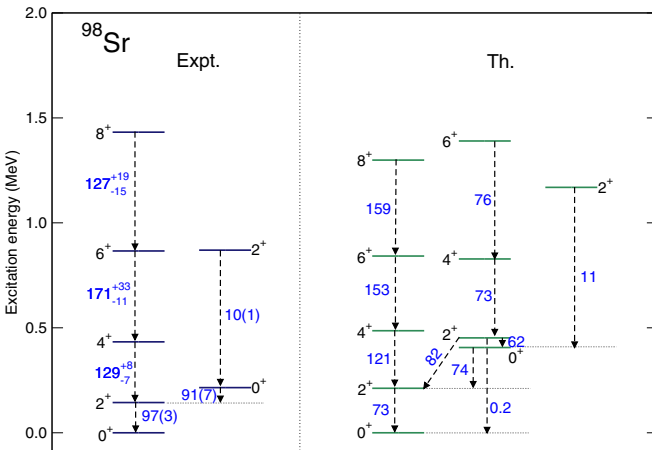

FIG. 19. The same as in Fig. 17, but for the ^{98}Sr nucleus. Data have been taken from Ref. [7].

TABLE I. Fraction (in units of percent) of the three configurations $[n = 0]$, $[n = 1]$, and $[n = 2]$ in the wave functions of the low-lying states of ^{98}Sr shown in Fig. 19.

	$[n = 0]$	$[n = 1]$	$[n = 2]$
0_1^+	2.4	60.6	37.0
0_2^+	1.9	37.6	60.5
2_1^+	0.9	39.3	59.9
2_2^+	1.0	67.2	31.9
2_3^+	4.7	75.9	19.5
4_1^+	0.2	16.8	83.0
4_2^+	0.8	85.6	13.6
6_1^+	0.0	8.2	91.8
6_2^+	0.4	90.9	8.7
8_1^+	0.0	4.6	95.4

H. Detailed comparison of low-energy spectra

So far, we have discussed some key observables as functions of neutron number. In this section, by means of the comparison with the available experimental data, we demonstrate that the mapping procedure is also able to describe the detailed band structure and decay patterns for the $N = 60$ isotones ^{104}Ru, ^{100}Zr, and ^{98}Sr. To this end, the energy levels have been classified into bands according to their dominant $E2$ decay patterns. The level scheme for ^{102}Mo is strikingly similar to that for ^{104}Ru and is not discussed in what follows.

1. ^{104}Ru

The level scheme shown in Fig. 17 for ^{104}Ru corresponds to a typical γ-soft spectra. The 2_2^+, which is likely the bandhead of the quasi-γ band, lies close to the 4_1^+ level. It also exhibits the $E2$ decay to the 2_1^+ state which is comparable to the
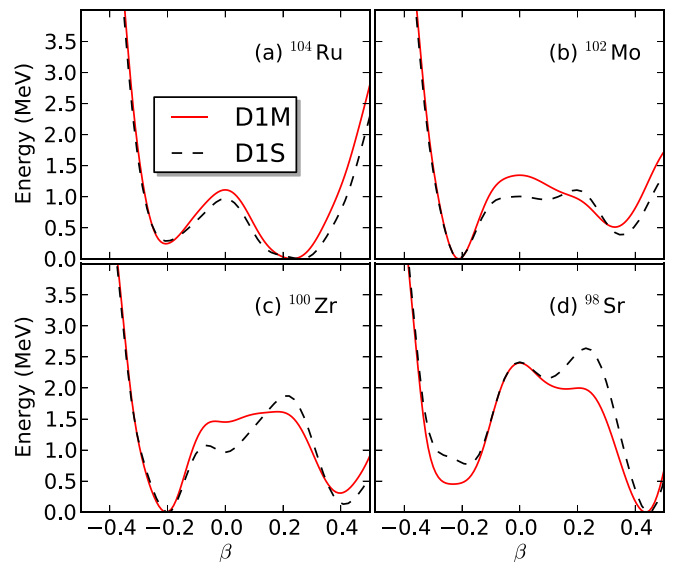

FIG. 20. The SCMF deformation-energy curves for the $N = 60$ isotones (a) ^{104}Ru, (b) ^{102}Mo, (c) ^{100}Zr, and (d) ^{98}Sr as functions of axial deformation parameter β (with $\gamma = 0°$), calculated with the Gogny D1S and D1M parametrizations.
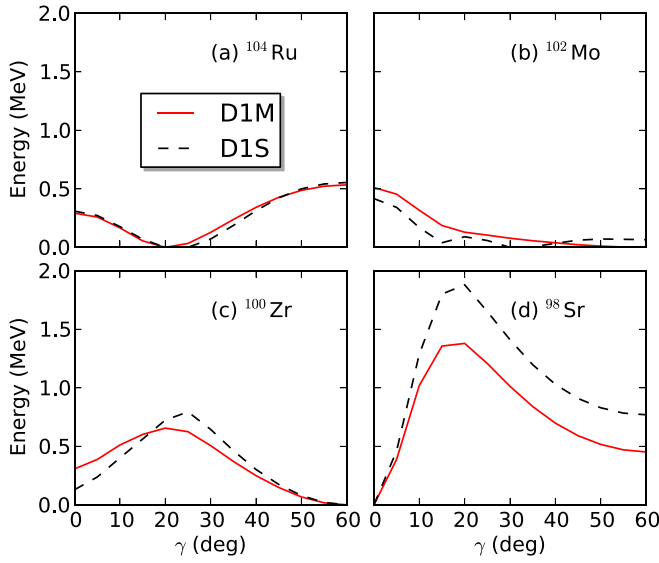
FIG. 21. The same as in Fig. 20, but as functions of nonaxial deformation parameter γ with a β value corresponding to the minimum at each γ value.

$B(E2; 2_1^+ \rightarrow 0_1^+)$ transition strength. The energy spacing in the sequence 2_2^+, 3_1^+, 4_2^+, 5_1^+, and 6_2^+ is rather constant. Like for other Ru isotopes, the quasi-γ spectra obtained for ^{104}Ru suggests that this system is somewhat in between the rigid-triaxial [65] and the γ-unstable [66] limits. Let us remark that the quasi-γ band systematics can only be reproduced by including the three-boson term in the IBM Hamiltonian [33]. The previous results compare well with those obtained

by using the five-dimensional (5D) collective Hamiltonian approach, based on the deformed Nilsson potential and the Strutinsky's shell correction [67].

2. ^{100}Zr

Experimentally the nucleus ^{100}Zr, shown in Fig. 18, is characterized by the 0_2^+ and 2_1^+ levels being rather close in energy and connected by a strong $E2$ transition probability of 67 ± 7 W.u. On the other hand, our calculations overestimate the 0_2^+ excitation energy, which is much higher than the 2_1^+ energy level and also higher than the experimental counterpart and is even above the 2_2^+ level. This is probably a consequence of strong level repulsion between the 0^+ states, since the mixing strength $\omega = 0.1$ MeV might be too large for this particular example. Also, the calculated $B(E2; 0_2^+ \rightarrow 2_1^+) = 0.9$ W.u. is too small compared with the experimental data. The too-small $E2$ transition strength reflects that these states have different characters: 31% (69%) of the wave function of the 0_2^+ (2_1^+) state is composed of the oblate $[n = 1]$ configuration.

Our calculations predict a third-lowest band based on the 2_3^+ state, which resembles a quasi-γ band but shows the level structure of the rigid-triaxial rotor [65]. The band built on the 0_3^+ state is also overestimated, again due to strong level repulsion between the 0^+ states.

3. ^{98}Sr

Figure 19 depicts the level scheme for the nucleus ^{98}Sr. The fractions of the near-spherical $[n = 0]$, oblate $[n = 1]$, and prolate $[n = 2]$ configurations introduced for this nucleus are given in Table I. Although the level scheme is somewhat similar to that obtained for ^{100}Zr, the agreement
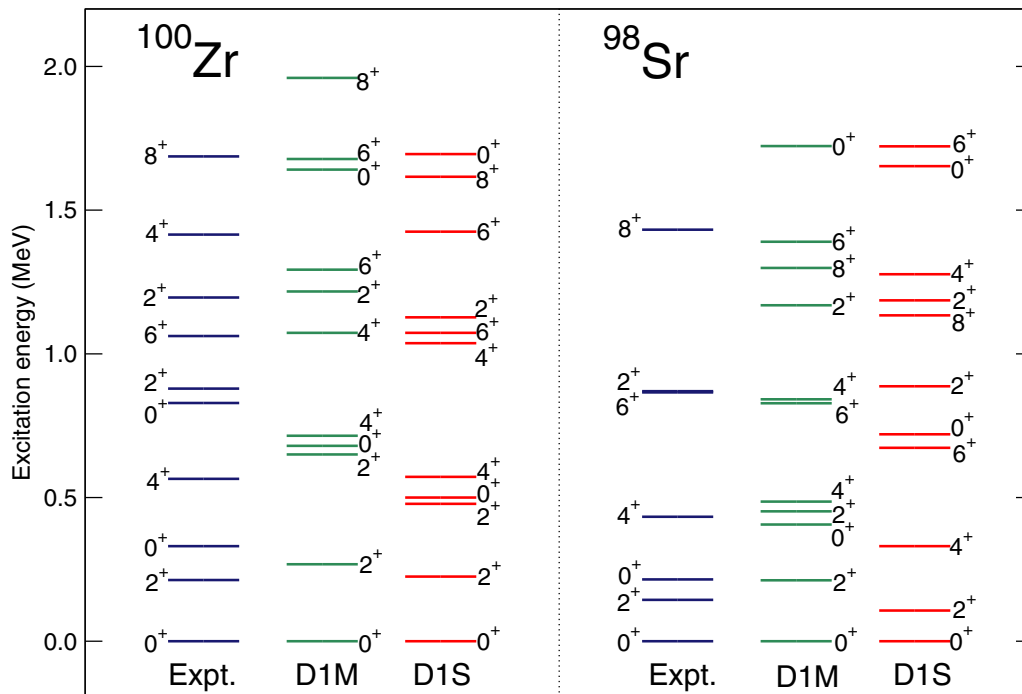

FIG. 22. Comparison of the low-energy spectra for the ^{100}Zr and ^{98}Sr nuclei calculated with the parametrizations D1M and D1S of the Gogny-EDF. The experimental data are also shown for reference.

with experiment is better. From Table I, one sees that the 0_1^+ (0_2^+) state is dominated by the oblate [$n = 1$] (prolate [$n = 2$]) configuration. However, the prolate [$n = 2$] (oblate [$n = 1$]) configuration becomes more dominant for higher angular momentum, which is compatible with the empirical systematics [8]. The excitation energy of the 0_2^+ state is overestimated but the strong decay to the 2_1^+ state is consistent with the experiment and reflects the large mixing between these two states. As can be seen from Table I, the content of the corresponding wave functions is similar. Experimentally there is a large energy gap between the 2_2^+ and 0_2^+ states. However, in our calculations both states are close in energy and are connected by a strong $E2$ decay rate (62 W.u.). On the other hand, the theoretical $B(E2; 2_3^+ \rightarrow 0_2^+)$ value of 11 W.u. agrees better with the experimental $B(E2; 2_2^+ \rightarrow 0_2^+)$ value. Let us mention that the quality of the agreement between our results and the experimental data is similar to that obtained recently using the 5D collective Hamiltonian approach based on the Gogny-D1S EDF [7].

I. Sensitivity tests

As pointed out in previous sections, there are two major factors which could affect the description of the energy spectra, especially those of the excited 0^+ states: one is the choice of the particular version of the EDF, and the other is the choice of the mixing interaction strength ω. In this section, we check the sensitivity of our results to these two factors.

First, we show in Figs. 20 and 21 the SCMF deformation-energy curves for the $N = 60$ isotones [(a)^{104}Ru, (b) ^{102}Mo, (c) ^{100}Zr, and (d) ^{98}Sr] calculated with the D1S and D1M parametrizations of the Gogny-EDF, as functions of the axial deformation parameter β (with $\gamma = 0°$) and the nonaxial deformation parameter γ (with β corresponding to the minimum at each γ value), respectively. In ^{104}Ru [Figs. 20(a) and 21(a)] and ^{102}Mo [Figs. 20(b) and 21(b)], we do observe no striking differences in the topology of the SCMF energy surfaces computed with the D1S and D1M parametrizations. In ^{100}Zr and ^{98}Sr, on the contrary, there are notable differences, especially, in the energies of prolate and oblate minima and in the γ softness.

Regarding the ^{100}Zr and ^{98}Sr nuclei, we compare in Fig. 22 the energy spectra obtained with the parameters deduced from the D1S and D1M energy surfaces. In Fig. 22, the results based on the D1S interaction suggest that, in both ^{100}Zr and ^{98}Sr, the energy levels for the yrast states, which are mainly composed of the oblate global minimum (see also Fig. 13), are more compressed than those based on the D1M interaction. The excitation energies of the nonyrast states, e.g., the 0_2^+ and 2_2^+ states, which are mainly coming from the second-lowest prolate mean-field minimum, are rather dependent on the choice of the EDF. This is corroborated by the SCMF results shown in panels (c) [(d)] of Figs. 20 and 21, where one sees that the energy difference between the prolate and oblate mean-field minima is in the case of the D1M force larger (smaller) than in the case of the D1S force.

Second, we display in Fig. 23 the excitation energy of the 2_1^+, 4_1^+, 0_2^+, and 2_2^+ states, calculated within the configuration-mixing IBM, as a function of the mixing interaction strength ω
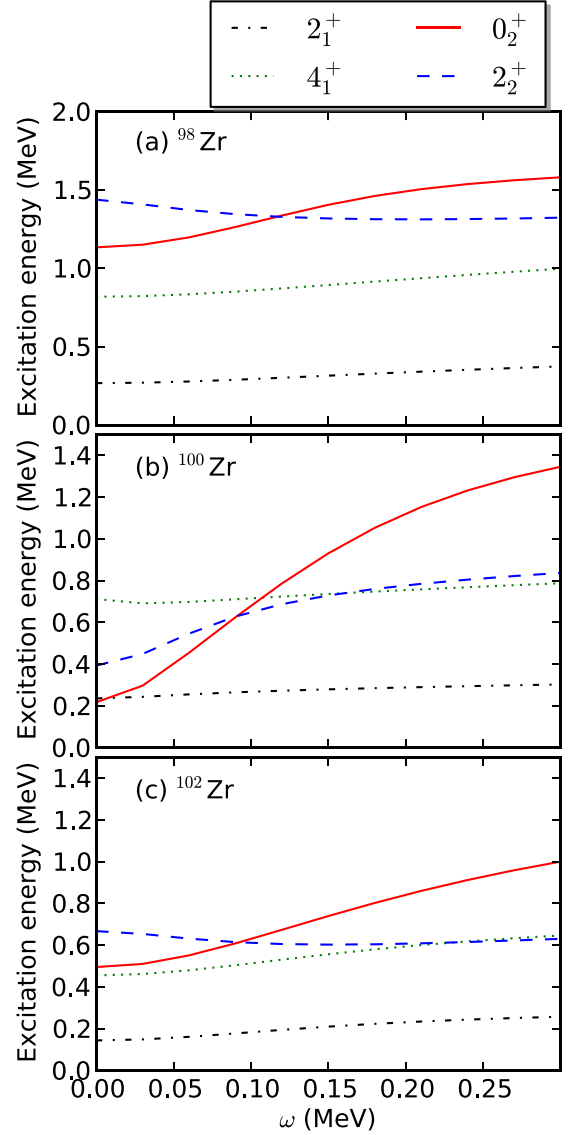

FIG. 23. Excitation energies of the 2_1^+, 4_1^+, 0_2^+, and 2_2^+ states of (a) ^{98}Zr, (b) ^{100}Zr, and (c) ^{102}Zr, as functions of the mixing interaction strength ω. Calculations are based on the parametrization D1M of the Gogny-EDF.

for ^{98}Zr [Fig. 23(a)], ^{100}Zr [Fig. 23(b)], and ^{102}Zr [Fig. 23(c)]. Calculations are based on the parametrization D1M of the Gogny-EDF. The energies of the yrast (2_1^+ and 4_1^+) states stay almost constant with ω, whereas those of the nonyrast (0_2^+ and 2_2^+) states are more sensitive to ω. For ^{98,100}Zr, the chosen value $\omega = 0.1$ MeV seems to be too large to explain the experimental 0_2^+ level energies of 854 and 331 keV, respectively [64]. For ^{102}Zr, on the other hand, a much larger strength ω could be required to account for the experimental 0_2^+ energy of 895 keV.

IV. CONCLUDING REMARKS

In this work, we study the shape evolution and coexistence in the neutron-rich nuclei $^{98-114}$Ru, $^{96-112}$Mo, $^{94-110}$Zr, and $^{92-108}$Sr. We have resorted to the SCMF-to-IBM mapping

procedure based on the Gogny-D1M EDF. The IBM parameters derived from such a procedure have been used to compute the spectroscopic properties of the nuclei considered. To keep our analysis as simple as possible, several approximations have been made. Our method describes reasonably well the evolution of the low-lying yrast and nonyrast states. Our results for Ru and Mo nuclei suggest many γ-soft examples while some vivid examples of coexistence between strongly deformed prolate and weakly deformed oblate shapes have been found for the Zr and Sr nuclei.

Our calculations describe well the rapid structural change between $N = 58$ and 60 in Zr and Sr nuclei. The analysis of the Gogny-D1M and mapped IBM energy surfaces as well as the wave functions of the 0_1^+ and 0_2^+ states reveals that the sudden lowering of the energy levels from $N = 58$ to 60 in those nuclei is the consequence of the onset of large prolate deformations. From Fig. 13, many of the Zr and Sr nuclei from $N = 60$ until around the neutron midshell $N \approx 66$ exhibit a prolate ground state while their 0_2^+ states are dominated by the oblate configuration. On the other hand, an oblate ground state is found for the heavier isotopes near $N = 70$.

We also point out several discrepancies between our predictions and the available experimental data. In particular, for many of the considered nuclei, the 0_2^+ excited state is predicted to be too high. In Mo isotopes, for example, the 0_2^+ energy level is systematically overestimated since the mixing is not introduced in most of the isotopes. The 0_2^+ excitation energy is neither well described at $N = 60$ and 62 in the case of Zr and Sr chains. This discrepancy could be related to the particular version of the Gogny-EDF employed in our calculations. In the case of ^{98}Mo, for example, the SCMF energy surface displays only one minimum whereas previous Skyrme-HF + BCS calculations [5] have found two minima. However, a second source for the discrepancy could also be the assumptions made at the IBM level. For example, the simplified form of the unperturbed Hamiltonian and a constant mixing strength may not be realistic enough for all studied nuclei. One could also use a different boson model space. Within this context, some refinement is still required to better constrain the IBM Hamiltonian. For example, both particle and hole pairs have been mapped onto the same boson image. However, a more realistic formulation would consider a single boson Hamiltonian where both particle-like and hole-like bosons are taken into account, rather than invoking several different unperturbed Hamiltonians. Nevertheless, we stress that the mapping procedure considered allows a systematic and computationally feasible description of medium-mass and heavy nuclei with several coexisting shapes. The method can also be used to predict the spectroscopic properties of unexplored nuclei.

[1] K. Heyde and J. L. Wood, Rev. Mod. Phys. **83**, 1467 (2011).

[2] T. Sumikama, K. Yoshinaga, H. Watanabe, S. Nishimura, Y. Miyashita, K. Yamaguchi, K. Sugimoto, J. Chiba, Z. Li, H. Baba *et al.*, Phys. Rev. Lett. **106**, 202501 (2011).

[3] M. Albers, N. Warr, K. Nomura, A. Blazhev, J. Jolie, D. Mücher, B. Bastin, C. Bauer, C. Bernards, L. Bettermann *et al.*, Phys. Rev. Lett. **108**, 062701 (2012).

[4] M. Albers, K. Nomura, N. Warr, A. Blazhev, J. Jolie, D. Mücher, B. Bastin, C. Bauer, C. Bernards, L. Bettermann *et al.*, Nucl. Phys. A **899**, 1 (2013).

[5] T. Thomas, K. Nomura, V. Werner, T. Ahn, N. Cooper, H. Duckwitz, M. Hinton, G. Ilie, J. Jolie, P. Petkov *et al.*, Phys. Rev. C **88**, 044305 (2013).

[6] F. Browne, A. Bruce, T. Sumikama, I. Nishizuka, S. Nishimura, P. Doornenbal, G. Lorusso, P.-A. Sderstrm, H. Watanabe, R. Daido *et al.*, Phys. Lett. B **750**, 448 (2015).

[7] E. Clément, M. Zielińska, A. Görgen, W. Korten, S. Péru, J. Libert, H. Goutte, S. Hilaire, B. Bastin, C. Bauer *et al.*, Phys. Rev. Lett. **116**, 022701 (2016).

[8] J. Park, A. B. Garnsworthy, R. Krücken, C. Andreoiu, G. C. Ball, P. C. Bender, A. Chester, A. Close, P. Finlay, P. E. Garrett *et al.*, Phys. Rev. C **93**, 014315 (2016).

[9] K. Sieja, F. Nowacki, K. Langanke, and G. Martínez-Pinedo, Phys. Rev. C **79**, 064310 (2009).

[10] S. Lalkovski and P. Van Isacker, Phys. Rev. C **79**, 044307 (2009).

[11] M. Böyükata, P. Van Isacker, and I. Uluer, J. Phys. G **37**, 105102 (2010).

[12] R. Rodríguez-Guzmán, P. Sarriguren, L. M. Robledo, and S. Perez-Martin, Phys. Lett. B **691**, 202 (2010).

[13] R. Rodríguez-Guzmán, P. Sarriguren, and L. M. Robledo, Phys. Rev. C **82**, 044318 (2010).

[14] H. Mei, J. Xiang, J. M. Yao, Z. P. Li, and J. Meng, Phys. Rev. C **85**, 034321 (2012).

[15] J. Xiang, Z. P. Li, Z. X. Li, J. M. Yao, and J. Meng, Nucl. Phys. A **873**, 1 (2012).

[16] T. R. Rodríguez, Phys. Rev. C **90**, 034306 (2014).

[17] P. Sarriguren, Phys. Rev. C **91**, 044304 (2015).

[18] P. Federman and S. Pittel, Phys. Lett. B **69**, 385 (1977).

[19] P. Federman and S. Pittel, Phys. Lett. B **77**, 29 (1978).

[20] J. Skalski, S. Mizutori, and W. Nazarewicz, Nucl. Phys. A **617**, 282 (1997).

[21] E. Caurier, G. Martínez-Pinedo, F. Nowacki, A. Poves, and A. P. Zuker, Rev. Mod. Phys. **77**, 427 (2005).

[22] M. Bender, P.-H. Heenen, and P.-G. Reinhard, Rev. Mod. Phys. **75**, 121 (2003).

[23] D. Vretenar, A. V. Afanasjev, G. Lalazissis, and P. Ring, Phys. Rep. **409**, 101 (2005).

[24] T. Nikšić, D. Vretenar, and P. Ring, Prog. Part. Nucl. Phys. **66**, 519 (2011).

[25] P. Bonche, H. Flocard, and P.-H. Heenen, Nucl. Phys. A **443**, 39 (1985).

[26] G. Lalazissis and M. Sharma, Nucl. Phys. A **586**, 201 (1995).

[27] P. Ring and P. Schuck, *The Nuclear Many-Body Problem* (Springer-Verlag, Berlin, 1980).

[28] R. Rodríguez-Guzmán, J. L. Egido, and L. M. Robledo, Nucl. Phys. A **709**, 201 (2002).

[29] K. Nomura, N. Shimizu, and T. Otsuka, Phys. Rev. Lett. **101**, 142501 (2008).

[30] F. Iachello and A. Arima, *The Interacting Boson Model* (Cambridge University Press, Cambridge, 1987).

[31] K. Nomura, N. Shimizu, and T. Otsuka, Phys. Rev. C **81**, 044307 (2010).

[32] K. Nomura, T. Otsuka, N. Shimizu, and L. Guo, Phys. Rev. C **83**, 041302 (2011).

[33] K. Nomura, N. Shimizu, D. Vretenar, T. Nikšić, and T. Otsuka, Phys. Rev. Lett. **108**, 132501 (2012).

[34] K. Nomura, R. Rodríguez-Guzmán, and L. M. Robledo, Phys. Rev. C **92**, 014312 (2015).

[35] K. Nomura, R. Rodríguez-Guzmán, L. M. Robledo, and N. Shimizu, Phys. Rev. C **86**, 034322 (2012).

[36] K. Nomura, R. Rodríguez-Guzmán, and L. M. Robledo, Phys. Rev. C **87**, 064313 (2013).

[37] K. Nomura, T. Otsuka, and P. Van Isacker, J. Phys. G **43**, 024008 (2016).

[38] P. Van Isacker and G. Puddu, Nucl. Phys. A **348**, 125 (1980).

[39] M. Sambataro and G. Molnár, Nucl. Phys. A **376**, 201 (1982).

[40] J. E. García-Ramos, K. Heyde, R. Fossion, V. Hellemans, and S. De Baerdemacker, Eur. Phys. J. A **26**, 221 (2005).

[41] P. Van Isacker and B. Sorgunlu, Nucl. Phys. A **808**, 27 (2008).

[42] J. Decharge, M. Girod, and D. Gogny, Phys. Lett. B **55**, 361 (1975).

[43] S. Goriely, S. Hilaire, M. Girod, and S. Péru, Phys. Rev. Lett. **102**, 242501 (2009).

[44] R. Rodríguez-Guzmán, P. Sarriguren, L. M. Robledo, and J. E. García-Ramos, Phys. Rev. C **81**, 024310 (2010).

[45] R. Rodríguez-Guzmán, L. M. Robledo, and P. Sarriguren, Phys. Rev. C **86**, 034336 (2012).

[46] L. M. Robledo and P. A. Butler, Phys. Rev. C **88**, 051302 (2013).

[47] R. Rodríguez-Guzmán and L. M. Robledo, Phys. Rev. C **89**, 054310 (2014).

[48] L. M. Robledo, J. Phys. G **42**, 055109 (2015).

[49] J. F. Berger, M. Girod, and D. Gogny, Nucl. Phys. A **428**, 23 (1984).

[50] L. M. Robledo, R. R. Rodríguez-Guzmán, and P. Sarriguren, Phys. Rev. C **78**, 034314 (2008).

[51] J. N. Ginocchio and M. W. Kirson, Nucl. Phys. A **350**, 31 (1980).

[52] T. Otsuka, A. Arima, F. Iachello, and I. Talmi, Phys. Lett. B **76**, 139 (1978).

[53] T. Otsuka, A. Arima, and F. Iachello, Nucl. Phys. A **309**, 1 (1978).

[54] P. D. Duval and B. R. Barrett, Phys. Lett. B **100**, 223 (1981).

[55] T. Mizusaki and T. Otsuka, Prog. Theor. Phys. Suppl. **125**, 97 (1996).

[56] F. Iachello, Phys. Rev. Lett. **53**, 1427 (1984).

[57] A. Bohr and B. M. Mottelsson, *Nuclear Structure* (Benjamin, New York, 1975), Vol. 2.

[58] A. Frank, P. Van Isacker, and C. E. Vargas, Phys. Rev. C **69**, 034323 (2004).

[59] W. Nazarewicz, Phys. Lett. B **305**, 195 (1993).

[60] K. Nomura, Ph.D. thesis, University of Tokyo, 2012.

[61] E. Chabanat, P. Bonche, P. Haensel, J. Meyer, and R. Schaeffer, Nucl. Phys. A **627**, 710 (1997).

[62] http://www-phynu.cea.fr/science_en_ligne/carte_potentiels_microscopiques/carte_potentiel_nucleaire_eng.htm.

[63] E. Chabanat, P. Bonche, P. Haensel, J. Meyer, and R. Schaeffer, Nucl. Phys. A **635**, 231 (1998).

[64] Brookhaven National Nuclear Data Center, http://www.nndc.bnl.gov

[65] A. S. Davydov and G. F. Filippov, Nucl. Phys. **8**, 237 (1958).

[66] L. Wilets and M. Jean, Phys. Rev. **102**, 788 (1956).

[67] J. Srebrny, T. Czosnyka, C. Droste, S. Rohoziński, L. Próchniak, K. Zajac, K. Pomorski, D. Cline, C. Wu, A. Bäcklin *et al.*, Nucl. Phys. A **766**, 25 (2006).